Published in Contributions to Mineralogy and Petrology 157, issue 4, 453-472, 2009
which should be used for any reference to this work

Pyroxenite xenoliths from Marsabit (Northern Kenya): evidence for different magmatic events in the lithospheric mantle and interaction between peridotite and pyroxenite

Benjamin Kaeser · Bettina Olker · Angelika Kalt · Rainer Altherr · Thomas Pettke

Abstract Garnet-bearing and garnet-free pyroxenite xenoliths from Quaternary basanites of Marsabit, northern Kenya, were analysed for microstructures and mineral compositions (major and trace elements) to constrain the thermal and compositional evolution of the lithospheric mantle in this region. Garnet-bearing rocks are amphibole-bearing websterite with ~5–10 vol% orthopyroxene. Clinopyroxene is LREE-depleted and garnet has high HREE contents, in agreement with an origin as cumulates from basaltic mantle melts. Primary orthopyroxene inclusions in garnet suggest that the parental melts were orthopyroxene-saturated. Rock fabrics vary from weakly to strongly deformed. Thermobarometry indicates extensive decompression and cooling (~970–1,100°C at ~2.3–2.6 GPa to ~700–800°C at ~0.5–1.0 GPa) during deformation, best interpreted as pyroxenite intrusion into thick Paleozoic continental lithosphere subsequently followed by continental rifting (i.e., formation of the Mesozoic Anza Graben). During continental rifting, garnet websterites were decompressed (garnet-to-spinel transition) and experienced the same *P–T* evolution as their host peridotites. Strongly deformed samples show compositional overlaps with cpx-rich, initially garnet-bearing lherzolite, best explained by partial re-equilibration of peridotite and pyroxenite during deformation and mechanical mingling. In contrast, garnet-free pyroxenites include undeformed, cumulate-like samples, indicating that they are younger than the garnet websterites. Major and trace element compositions of clinopyroxene and calculated equilibrium melts suggest crystallisation from alkaline basaltic melt similar to the host basanite, which suggests formation in the context of alkaline magmatism during the development of the Kenya rift.

Keywords Pyroxenite · Mantle xenoliths · Thermobarometry · Trace elements · East African rift

B. Kaeser · A. Kalt
Institut de Géologie et d'Hydrogéologie,
Université de Neuchâtel, Rue Emile-Argand 11,
2009 Neuchâtel, Switzerland

B. Olker · R. Altherr
Mineralogisches Institut, Universität Heidelberg,
Im Neuenheimer Feld 236, 69120 Heidelberg, Germany

T. Pettke
Institut für Geologie, Universität Bern,
Baltzerstrasse 1, 3012 Bern, Switzerland

B. Kaeser (✉)
BSL Baustofflabor AG, Postfach,
3661 Uetendorf, Switzerland
e-mail: b.kaeser@baustofflabor.ch; benjamin.kaeser@unine.ch

Introduction

Occurrences of mantle rock almost always include minor amounts of pyroxenite, indicating that mafic lithologies represent important heterogeneities in the otherwise peridotitic mantle (for recent reviews, see Pearson et al. 2003; Bodinier and Godard 2003; Downes 2007). Most tectonically exhumed ultramafic massifs and ophiolite complexes, which allow for large-scale structural studies, exhibit mm–dm-sized websterite and/or clinopyroxenite bands or layers, typically aligned parallel to the main foliation of the

tectonised peridotite (Bodinier and Godard 2003). Among these, most are spinel-bearing while garnet-bearing pyroxenite is rarer but occurs in several localities.

With respect to their petrogenesis, there is general consensus that most mantle pyroxenites crystallised from mantle-derived melts (or fluids). However, based on geochemical arguments, a few pyroxenite occurrences have been interpreted to represent remnants of subducted mafic oceanic crust, streaked out during recycling through the convecting asthenosphere, until re-incorporated into the lithosphere (e.g., Allègre and Turcotte 1986; Kornprobst et al. 1990). However, the majority of pyroxenites are well explained by mantle melts propagating along hydraulically opened cracks and crystallising cumulates/segregates (the actual pyroxenites), which may evolve later into parallel layers by plastic (sub-solidus) deformation (Bodinier and Godard 2003; Downes 2007, and references therein).

In addition to magmatic differentiation, the formation of mantle pyroxenites is complicated by interaction between the parental melts and surrounding wall-rock peridotite on the one hand, and by later recrystallisation and partial re-equilibration at sub-solidus conditions on the other hand. This often obliterates the 'primary' composition of pyroxenite (Bodinier et al. 1987; Rivalenti et al. 1995; Garrido and Bodinier 1999; Zanetti et al. 1999; Litasov et al. 2000; Liu et al. 2005). In the following, we will present a detailed study of two groups of pyroxenite xenoliths from Quaternary basanitic maars, erupted on the Marsabit shield volcano in the context of the Kenya rift magmatism (e.g., Henjes-Kunst and Altherr 1992). On the basis of detailed microstructural observations, thermobarometry calculations and major and trace element compositions of minerals, we will show that the mantle beneath Marsabit experienced at least two events of addition of mafic material that probably formed in different tectonic settings and experienced variable degrees of reaction and re-equilibration with their host peridotite.

Petrography

Following the classification of the Marsabit peridotites of Kaeser et al. (2006; Groups I to IV), the mafic xenoliths will be subdivided into Group V (garnet websterite; 11 samples) and Group VI (garnet-free pyroxenite; four samples). Estimates of modal compositions are provided in Table 1 (based on point counting; see table caption for details). Microstructures are illustrated in Figs. 1a–h and 2a–d. A detailed petrographic description of each sample is given in the electronic appendix A1. The following mineral abbreviations will be used: grt for garnet; opx-I, cpx-I, ol-I, and spl-I for first generation (i.e., porphyroclasts or microstructurally equilibrated grains) orthopyroxene, clinopyroxene, olivine and spinel, respectively; suffix 'IIa' indicates neoblasts in porphyroclastic rocks, whereas 'IIb' indicates symplectitic minerals resulting from garnet-breakdown. The subscript 'm' indicates minerals in late-stage metasomatic plagioclase-bearing reaction zones.

Group V: garnet websterites

Grt websterite is mainly composed of cpx ($\sim$1–5 mm) and grt (cm-sized). Opx contents strongly vary on the thin section scale, but are generally $\geq$5 vol% with higher abundances in more strongly deformed samples (Table 1). Several samples contain cm-wide orthopyroxenitic domains (Fig. 1e). Primary olivine is confined to these opx-rich domains, where it occurs as small (< 1 mm), commonly deformed interstitial grains (Fig. 1e).

All samples show at least some deformation (Fig. 1a–e) and are microstructurally similar to grt pyroxenite layers described from exhumed peridotite massifs (e.g., Lherz: Conquéré 1977; the Ligurides: Montanini et al. 2006; Zabargad: Piccardo et al. 1988; Malenco: Müntener and Hermann 1996). The degree of deformation ranges from undulous extinction in pyroxenes in weakly deformed samples (Fig. 1a, b), via samples with porphyroclastic up to protomylonitic microstructures (Fig. 1c–e). The pyroxene microstructures are strikingly similar to those observed in Group I lherzolites (Kaeser et al. 2006). Cpx-I porphyroclasts always contain opx exsolution lamellae (Fig. 1b). Occasionally bent lamellae indicate that exsolution pre-dated deformation. One sample (Ke 1958/2; not shown) shows a granular microstructure and is composed of strain- and exsolution-free polygonal pyroxenes, similar to the statically recrystallised (grt)-spl lherzolites of Group II (Kaeser et al. 2006).

In most samples, grt is partially replaced by symplectitic spl-IIb + opx-IIb + cpx-IIb ($\pm$Ti-pargasite). Symplectite formation preferentially occurred in more strongly deformed samples and/or in opx-rich domains (Fig. 1c, e). In the latter, grt is commonly completely transformed to symplectite. The symplectites are microstructurally identical to those in Group I lherzolites, interpreted to have formed by a grt-breakdown reaction such as grt + ol = spl + opx + cpx (Kaeser et al. 2006). Reactant olivine, however, is only preserved in opx-rich domains.

Grt cores typically contain euhedral cpx-I (up to 0.5 mm; Fig. 1d) with opx exsolution lamellae. Of much smaller size (10–100 μm) are inclusions of rutile (needle-like), euhedral Ti-pargasite and opx (sometimes polyphase; Fig. 1f). Ti-pargasite (<5 vol%) also occurs outside grt, either as microstructurally equilibrated interstitial grains, as selvages replacing cpx-I, or within symplectite. Interstitial phlogopite and ilmenite (Fig. 1b) were found in

Table 1 Microstructures, modal composition and *P–T* evolution of pyroxenite xenoliths from Marsabit investigated in this study

Sample	Rock type	Group	Microstructure	Modal composition (vol%)[a]								*P–T* evolution *T* (°C)/*P* (Gpa)						
				grt	cpx	opx	ol	spl	amph	phl	TiOx	Method[b]	Mineral cores[c]			Mineral rims + neoblasts[d]		P_{max}[e]
771/1	grt websterite	V	Weakly deformed	27	70	2	–	–	>1	–	tr.	I	926 ± 50	/	1.46 ± 0.09	805 ± 57	/ 0.90 ± 0.14	1.40
771/2	grt websterite	V	Porphyroclastic	30	41	29	–	–	<1	–	–	I	926 ± 42	/	2.17 ± 0.03	748 ± 17	/ 0.87 ± 0.16	1.40
784/1	grt websterite	V	Weakly deformed	40	52	6	–	–	2	tr.	tr.	II and I[f]	1,011	/	2.34	835	/ 0.95	
1958/2	grt websterite	V	Granular recrystallised	31	62	7	<1	–	<1	–	–	I	970 ± 36	/	1.41 ± 0.05	1066 ± 46	/ 1.29 ± 0.04	1.39
1959/18	grt websterite	V	Porphyroclastic	27	49	21	>1	–	2	–	–	I	1,044 ± 81	/	2.31 ± 0.40	757 ± 35	/ 0.78 ± 0.11	1.44
1960/3	grt websterite	V	Porphyroclastic	38	55	7	–	–	<1	–	–	I	1,034 ± 46	/	2.45 ± 0.20	712 ± 48	/ 0.52 ± 0.10	1.38
1960/4	grt websterite	V	Porphyroclastic to protomylonitic	36	52	10	>1	–	<1	–	–	I	1,030 ± 55	/	2.48 ± 0.57	716 ± 49	/ 0.18 ± 0.12	1.36
1960/5	grt websterite	V	Porphyroclastic	25	54	20	<1	–	<1	tr.–	tr.	I	1,066 ± 46	/	2.51 ± 0.19	753 ± 17	/ 0.58 ± 0.22	1.42
1960/6	grt websterite	V	Porphyroclastic	31	50	15	>1	–	2	–	–	I	1,031 ± 41	/	2.45 ± 0.07	859 ± 20	/ 0.93 ± 0.09	–
1960/8	grt websterite	V	Porphyroclastic	49	44	7	<1	–	tr.	–	–	I	1,012 ± 32	/	2.37 ± 0.10	727 ± 21	/ 0.60 ± 0.06	1.41
1964	grt websterite	V	Protomylonitic	39	50	11	–	–	tr.	–	–	I	996 ± 11	/	2.31 ± 0.12	752 ± 91	/ 0.55 ± 0.15	1.49
726	spl-ol cpx-ite	VI	Weakly deformed	–	62	–	30	8	–	–	–							1.51
782/1	websterite	VI	Granular recrystallised	–	92	8	tr.	–	–	–	–	II	1,022 ± 68	/	1.2 (assumed)			
782/2	spl-ol cpx-ite	VI	Weakly deformed	–	91	<1	8	<1	–	–	–	II	1,015 ± 70	/	1.2 (assumed)			1.43
1973/2	spl-ol cpx-ite[7]	VI	Undeformed	–	91	–	8	>1	–	–	–							1.46

grt garnet, *cpx* clinopyroxene, *opx* orthopyroxene, *ol* olivine, *spl* spinel, *amph* amphibole, *phl* phlogopite, TiO_x Ti oxides (rutile and ilmenite), *tr.* traces amounts (<0.1 vol%)

[a] Obtained by point counting; a relative uncertainty of ~25% was estimated for modal grt, cpx and opx given the large grain sizes, small sample sizes and strongly heterogeneous mineral distribution; modal composition include only first generation minerals; grt-breakdown products (symplectite) were added to modal garnet

[b] Method I = *T* based on Mg–Fe exchange between grt and opx combined with *P* based on the Al-in-opx (Brey and Köhler 1990); method II = *T* based on enstatite-diopside solvus thermometry (Brey and Köhler 1990), see Electronic Appendix A3 for further details

[c] *P–T* calculations based on the composition of opx-I, cpx-I and grt cores

[d] *P–T* calculations based on cpx-I, opx-I and grt rims, as well as cpx-IIa and opx-IIa (neoblasts) cores

[e] Maximum pressures based on the Cr-content of symplectitic spl-IIb (Carroll Webb and Wood 1986)

[f] *P–T* data from Henjes-Kunst and Altherr (1992)

[g] Xenolith contains an enclave of Group II (grt)-spl lherzolite

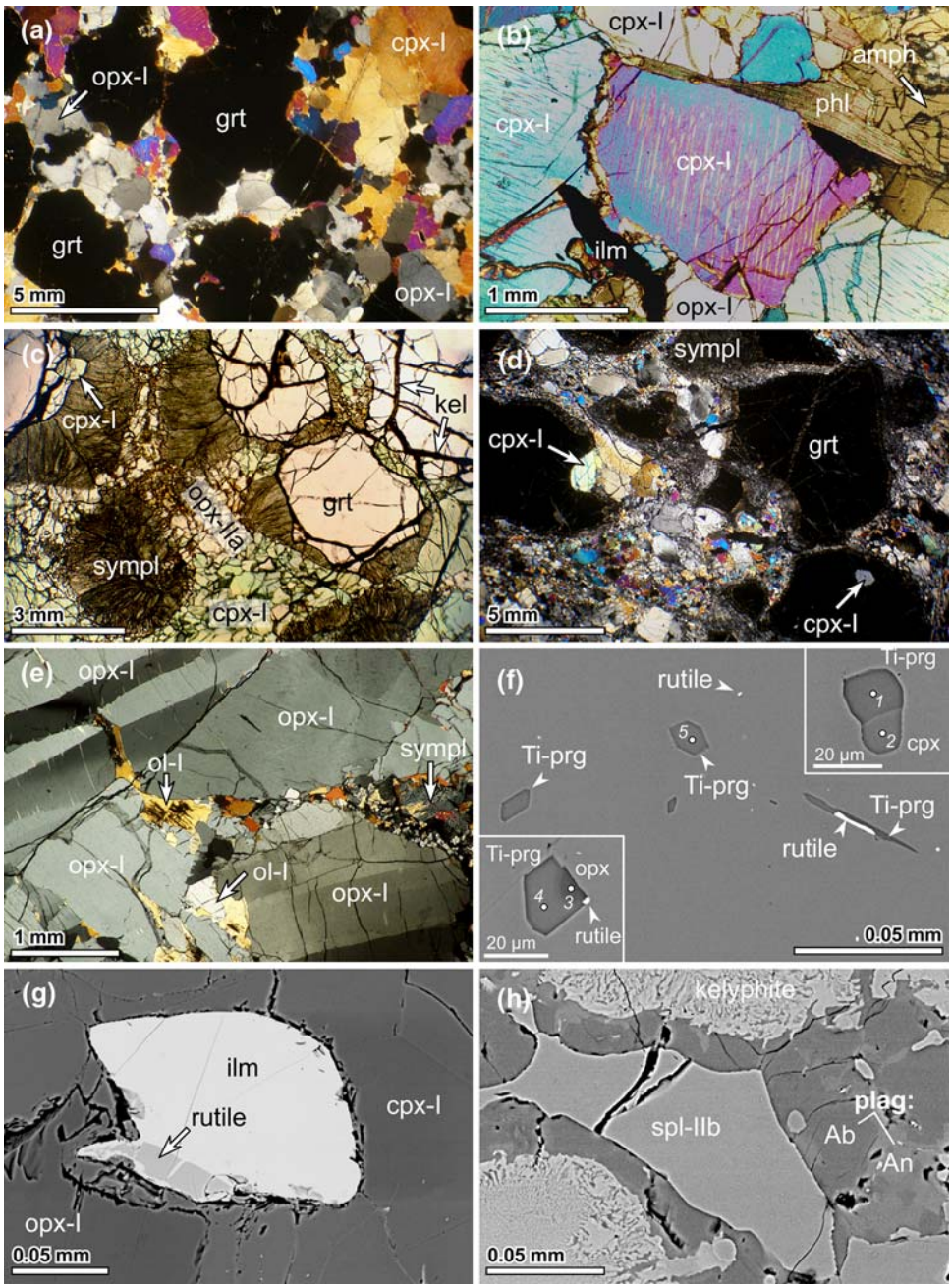

Fig. 1 Microstructures of Group V grt websterite xenoliths from Marsabit (**a**–**e** photomicrographs; **f**–**h** backscattered electron images): **a** weakly deformed grt websterite Ke 784/1 containing primary clinopyroxene (*cpx-I*), orthopyroxene (*opx-I*) and garnet (*grt*); **b** phlogopite (*phl*), amphibole (*amph*) and ilmenite (*ilm*) in textural equilibrium with primary exsolved cpx-I in weakly deformed grt websterite Ke 784/1; **c** texture-controlled transformation garnet and olivine (not preserved) to spl–opx–cpx symplectite (*sympl*) in porphyroclastic grt websterite Ke 1960/8: note that symplectite preferentially forms in opx-rich domains, whereas no reaction occurs at cpx–grt contacts. In turn, kelyphite forms along both grt grain boundaries and cracks, irrespective of adjacent phases; **d** protomylonitic fabric of grt websterite Ke 1964. Note primary subhedral cpx-I inclusions in grt; **e** strongly deformed opx-I (with cpx exsolution lamellae normal to kink bands) and interstitial olivine (*ol-I*) in protomylonitic grt websterite Ke 1960/4. Note that garnet transformed completely to spl–opx–cpx symplectite (*sympl*); **f** primary Ti-pargasite (*Ti–prg*), cpx, opx and rutile inclusions in garnet from weakly deformed grt websterite Ke 784/1 (*white dots* correspond to electron microprobe analyses listed in Table 3); **g** interstitial ilmenite mantling relic rutile (weakly deformed grt websterite Ke 784/1); **h** late-stage reaction zone in porphyroclastic grt websterite Ke 1059/18: kelyphitised garnet and plagioclase forming at the expense of spinel (*spl-IIb*). Note albite- (*Ab*) and anorthite-rich (*An*) domains of plagioclase

some samples, the latter occasionally enclosing rutile (Fig. 1g).

Finally, primary minerals are typically replaced along cracks and grain boundaries by late-stage, plagioclase-bearing reaction zones (Fig. 1h). Kelyphitic $pl_m + spl_m$ replaces garnet along grain boundaries and cracks. Further, $pl_m + cpx_m + spl_m + ol_m \pm$ kaersutite $\pm$ Ti oxide $\pm$ sulphide form at the expense of spl-opx-cpx symplectite. In addition, cpx_m and pl_m form rims on, or domains within cpx-I, cpx-IIa and/or cpx-IIb.

Group VI: grt-free pyroxenites

Grt-free pyroxenites include spl-ol clinopyroxenite (three samples) and spl-free websterite (1 sample). One clinopyroxenite (sample Ke 1973/2) is a composite xenolith enclosing an enclave of statically recrystallised Group II lherzolite (Kaeser et al. 2006). Clinopyroxenite samples show microstructures ranging from weakly deformed (undulous extinction, kink bands) to completely strain free, similar to ad-cumulates (Fig. 2a–c). Cpx-I contains abundant Fe–Ni–Cu sulphide and rare calcite inclusions. The websterite sample shows a granular fabric including large aggregates of cpx and opx, presumably representing former exsolved cpx-I porphyroclasts (Fig. 2d). Orthopyroxene is restricted to samples showing subsolidus features (exsolution lamellae, deformed fabrics).

Composition of minerals

Major and trace element compositions of minerals were analysed in situ using electron microprobe facilities at the Universities of Bern and Heidelberg, and the laser ablation-inductively coupled plasma mass spectrometry (LA-ICP-MS) facility at ETH Zürich, respectively. A full description of analytical methods is given elsewhere (Pettke et al. 2004; Kaeser et al. 2007). The results are summarised in Tables 2 (first generation minerals) and 3 (inclusions in grt). Representative trace element analyses are given in Table 4. A more extensive data set is given in the electronic Appendix A2.

Major elements: Group V grt websterites

The most important feature of all Group V grt websterites is that they show a clear correlation between mineral compositions and the degree of deformation: Mg# [atomic $Mg/(Mg + Fe_{tot})$] and Cr-contents of all major constituents (cpx, grt and opx) increase with increasing deformation, approaching and overlapping with the compositional range shown for the Group I (grt)-spl lherzolites (Kaeser et al. 2006).

Cpx of Group V xenoliths range from Cr diopside (more deformed samples) to Al augite (less deformed samples) with variable TiO_2 and Na_2O contents (0.2–1.1 and 1.2–3.7 wt%, respectively; Fig. 3a–c). These compositions are similar to grt pyroxenite suites from elsewhere (e.g., Wilshire and Shervais 1975; O'Reilly and Griffin 1987; Kopylova et al. 1995; Ho et al. 2000; Litasov et al. 2000; Table 2) but clearly different from typical alkali basalt-hosted cpx megacrysts (Fig. 3a–c). Grt is pyrope-rich ($Prp_{57–70}$) and grossular-poor ($Grs_{9–13}$), with strongly variable Cr_2O_3 contents (0.04–1.66 wt%; Table 2) and opx is Al-rich enstatite (Mg# of 80.2–91.5). Cpx-IIa and opx-IIa

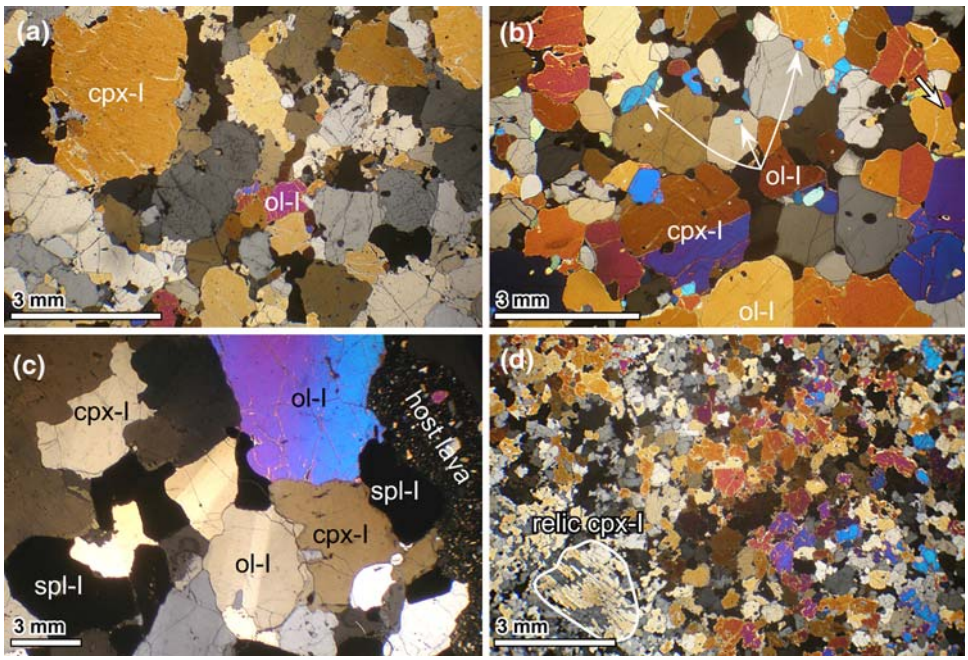

Fig. 2 Microstructures of Group VI garnet-free pyroxenites from Marsabit (photomicrographs). **a** Weakly deformed spl-ol clinopyroxenite Ke 782/2. Note ragged grain boundaries indicating sub-solidus grain boundary migration; **b** undeformed spl-ol clinopyroxenite Ke 1973/2. Note magmatic twinning (*orange-blue*) in the labelled cpx-I grain; **c** coarse-grained weakly deformed spl-ol clinopyroxenite Ke 726. Note kinkbands in olivine; **d** granular recrystallised websterite (sample Ke 782/1). Note lamellar intergrown opx and cpx (*white outlined*) most likely representing a former exsolved cpx-I porphyroclast

Table 2 Major element composition (ranges) of minerals in mafic xenoliths from Marsabit (concentrations in wt%)

Sample	Min.[a]	SiO_2	TiO_2	Al_2O_3	Cr_2O_3	FeO[a]	MnO	MgO	CaO	Na_2O	Mg#
Ke 771/1	Grt	40.6–41.7	0.00–0.22	22.3–23.4	0.04–0.20	13.7–15.3	0.22–0.49	16.0–17.7	3.59–4.29	0.00–0.09	65.7–72.0
(grt webs)	Cpx	51.2–54.1	0.39–0.69	6.52–9.44	0.03–0.22	3.10–4.42	0.00–0.13	11.8–14.0	17.7–18.5	3.13–3.91	83.2–86.1
weak def.	Opx	53.3–55.1	0.00–0.11	2.11–4.52	0.00–0.11	11.0–12.9	0.05–0.20	28.8–30.1	0.21–0.36	0.02–0.10	80.1–82.9
	Amph	42.1–42.7	2.25–3.05	15.0–16.2	0.10–0.34	4.07–4.53	0.00–0.08	14.7–15.6	10.1–10.8	3.94–4.51	80.4–82.3
Ke 771/2	Grt	41.3–42.4	0.01–0.19	22.6–23.7	0.19–0.67	9.83–12.1	0.31–0.93	17.7–19.8	3.65–4.14	0.00–0.06	72.3–78.7
(grt web)	Cpx	51.6–53.3	0.52–0.89	6.51–7.48	0.48–0.65	2.34–2.84	0.00–0.16	13.0–14.2	18.7–21.0	2.06–3.26	89.6–91.1
p.clastic	Opx	54.8–56.6	0.02–0.18	1.50–3.27	0.06–0.23	6.85–7.83	0.07–0.23	32.6–33.9	0.23–0.39	0.01–0.07	87.8–89.6
	Amph	41.7–43.4	2.62–3.50	14.7–16.3	0.29–0.36	2.63–2.94	0.02–0.09	15.9–16.8	10.8–11.3	3.88–4.31	87.1–88.9
Ke 784/1	Grt	40.9–42.3	0.02–0.22	22.1–23.2	0.17–0.44	12.3–14.0	0.22–0.57	17.1–18.6	4.19–4.91	0.00–0.07	70.4–74.4
(grt web)	Cpx	52.2–53.1	0.52–0.83	4.98–5.83	0.11–0.27	3.31–3.76	0.00–0.13	14.3–14.7	20.9–21.2	1.89–2.26	87.3–88.5
weak def.	Opx	53.7–54.8	0.12–0.23	3.82–5.12	0.00–0.11	8.26–9.13	0.03–0.21	31.1–31.9	0.27–0.40	0.02–0.08	85.9–87.0
	Amph	42.4–43.1	3.88–5.21	13.9–14.8	0.08–0.30	3.33–3.73	0.00–0.11	15.5–16.4	10.5–11.1	3.83–4.18	84.5–85.9
	Phl	37.6–37.9	6.80–7.04	14.1–15.0	0.29–0.37	7.82–8.05	0.00–0.04	17.5–17.9	0.01–0.03	1.01–1.10	79.7–80.3
	Ilm	0.01–0.03	57.4–59.0	0.25–0.44	0.12–0.33	27.6–31.8	0.26–0.41	10.0–12.4	0.04–0.23	n.d.	36.0–44.5
	Rut	0.01–0.03	98.6–99.5	0.11–0.17	0.16–0.21	0.38–0.45	0.00–0.02	0.00–0.01	0.06–0.08	n.d.	–
Ke 1958/2	Grt	41.9–42.6	0.03–0.18	22.9–23.7	0.16–0.34	8.49–9.37	0.40–0.67	19.8–20.9	4.45–4.85	0.00–0.05	79.6–80.8
(grt web)	Cpx	51.0–53.0	0.40–0.59	6.68–9.34	0.14–0.42	2.60–3.19	0.02–0.18	14.4–15.4	19.2–21.1	1.57–2.07	89.5–91.0
Granular	Opx	54.5–54.8	0.07–0.12	4.76–5.98	0.06–0.19	6.55–7.45	0.11–0.17	32.3–33.2	0.41–0.78	0.07–0.12	89.2–89.9
	Amph	42.0–42.5	2.03–2.65	15.5–16.8	0.25–0.54	2.82–3.35	0.04–0.18	16.3–17.0	10.3–10.6	3.10–3.55	85.9–88.2
Ke 1959/18	Grt	42.2–42.9	0.00–0.18	22.7–23.1	0.14–0.46	9.10–12.5	0.28–0.64	18.6–20.9	3.76–4.14	0.00–0.07	74.6–81.7
(grt web)	Cpx	53.0–54.1	0.61–0.80	6.61–8.89	0.25–0.44	2.23–2.95	0.00–0.13	12.7–14.2	18.1–19.3	2.80–3.69	89.0–91.3
p.clastic	Opx	54.0–56.4	0.04–0.18	2.28–5.01	0.06–0.23	7.32–8.57	0.07–0.22	32.1–33.3	0.26–0.48	0.02–0.10	87.1–88.9
	Amph	42.9–43.5	3.26–3.73	14.8–15.5	0.34–0.45	3.15–3.40	0.03–0.11	15.8–16.3	10.1–10.5	4.09–4.16	85.4–86.5
	Ol	40.5–41.2	n.d.	n.d.	n.d.	12.9–13.3	0.10–0.21	47.2–47.6	0.01–0.04	–	86.5–86.7
Ke 1960/3	Grt	41.6–42.6	0.10–0.25	22.8–23.6	0.27–0.38	8.13–9.11	0.29–0.38	19.8–20.8	4.35–4.96	0.01–0.08	81.2–85.0
(grt web)	Cpx	52.3–53.6	0.50–0.92	5.34–8.48	0.25–0.55	1.80–2.56	0.00–0.13	13.0–15.5	20.2–21.2	2.02–3.12	91.0–93.0
p.clastic	Opx	55.4–56.6	0.10–0.17	2.14–2.82	0.06–0.11	7.25–7.73	0.10–0.15	32.5–33.3	0.26–0.40	0.01–0.08	88.4–89.2
	Amph	43.1	3.61	15.5	0.35	2.98	0.05	15.6	10.8	3.69	86.8
Ke 1960/4	Grt	41.1–42.5	0.04–0.20	22.3–23.3	0.66–0.89	8.48–11.1	0.31–0.63	18.4–20.4	4.41–5.25	0.00–0.07	76.4–82.7
(grt web)	Cpx	51.7–54.0	0.42–0.74	4.33–7.70	0.49–0.79	1.48–2.43	0.02–0.12	13.6–15.5	20.6–22.5	1.19–2.82	91.5–94.5
p.clastic to	Opx	54.6–56.9	0.02–0.19	1.78–4.54	0.13–0.30	6.52–7.95	0.05–0.20	32.3–34.3	0.17–0.40	0.00–0.07	88.0–90.3
mylonitic	Ol	40.2–40.6	0.01–0.02	0.02–0.05	n.d.	11.1–11.5	0.07–0.17	46.3–46.9	0.13–0.15	0.01–0.02	87.8–88.3
	Amph	41.3–42.5	3.07–4.39	15.2–16.0	0.45–0.67	2.30–2.77	0.01–0.10	15.5–16.8	11.5–11.9	3.25–3.61	87.5–90.0
Ke 1960/5	Grt	41.7–42.7	0.04–0.26	22.8–23.8	0.13–0.53	8.55–10.4	0.25–0.51	19.1–20.6	4.21–4.79	0.00–0.07	76.9–82.3
(grt web)	Cpx	52.8–54.3	0.55–0.89	5.38–6.40	0.21–0.39	2.12–2.69	0.00–0.12	13.8–14.7	20.3–21.1	2.06–2.45	90.2–92.4
p.clastic	Opx	55.1–57.1	0.03–0.22	1.748–4.95	0.04–0.21	6.58–7.60	0.04–0.23	31.8–33.8	0.19–0.47	0.01–0.08	88.3–90.0
	Amph	42.3–43.0	2.88–4.15	15.5–16.2	0.32–0.49	2.26–2.66	0.01–0.08	15.6–16.5	10.7–11.1	3.52–4.18	88.0–90.0
Ke 1960/6	Grt	41.4–42.6	0.03–0.24	22.7–23.6	0.34–0.59	8.11–9.86	0.25–0.55	19.0–20.7	4.33–4.80	0.00–0.07	78.4–84.2
(grt web)	Cpx	52.0–52.9	0.69–1.10	6.04–7.21	0.44–0.58	1.97–2.32	0.03–0.09	14.0–14.8	20.1–20.8	2.00–2.47	91.8–92.7
p.clastic	Opx	54.7–56.7	0.07–0.24	5.12–5.43	0.08–0.27	6.12–6.86	0.06–0.23	32.8–34.4	0.24–0.46	0.03–0.10	89.6–90.8
	Amph	41.7–42.6	3.39–3.87	15.4–16.5	0.45–0.59	2.87–3.24	0.04–0.07	15.6–15.9	10.5–11.2	3.32–3.58	85.9–87.1
Ke 1960/8	Grt	41.8–42.4	0.05–0.12	23.1–23.7	1.32–1.66	8.22–10.2	0.29–0.61	18.4–20.1	4.99–5.21	0.01–0.06	76.3–81.3
(grt web)	Cpx	52.6–53.4	0.24–0.33	5.73–7.59	0.45–1.48	2.14–2.47	0.05–0.10	13.6–14.6	21.0–22.1	2.17–2.49	91.0–91.9
p.clastic	Opx	54.7–56.4	0.01–0.05	3.13–4.86	0.18–0.48	6.67–7.09	0.11–0.18	32.0–33.2	0.20–0.38	0.02–0.09	89.1–89.7
Ke 1964	Grt	42.1–43.0	0.03–0.10	23.8–24.3	0.78–1.14	6.92–8.67	0.26–0.42	18.8–21.2	4.49–5.38	0.00–0.08	78.2–85.6
(grt web)	Cpx	53.7–54.6	0.21–0.29	4.16–4.92	0.6–0.93	1.39–1.62	0.02–0.08	15.1–15.7	22.1–23.2	1.37–1.95	94.3–95.1
mylonitic	Opx	55.1–57.4	0.01–0.07	2.12–5.10	0.09–0.42	5.39–6.57	0.08–0.16	32.4–34.5	0.19–0.33	0.01–0.08	89.8–91.6
Ke 726	Cpx	48.2–48.7	1.13–1.49	8.48–8.94	0.00–0.08	5.72–6.37	0.08–0.18	12.9–14.2	19.9–20.5	1.03–1.24	78.9–81.0

Table 2 continued

Sample	Min.[a]	SiO_2	TiO_2	Al_2O_3	Cr_2O_3	FeO[a]	MnO	MgO	CaO	Na_2O	Mg#
(spl-ol	Ol	38.8–39.5	0.00–0.06	0.04–0.07	0.00–0.03	16.1–18.6	0.19–0.31	42.1–44.2	0.17–0.33	0.01–0.04	80.1–83.0
cpx-ite)	Spl	0.06–0.17	0.42–0.67	58.8–61.4	0.55–0.81	18.1–22.2	0.07–0.20	17.7–19.5	0.00–0.04	n.a.	58.9–65.7
Ke 782/1	Cpx	50.2–51.6	0.45–0.6	5.89–6.77	0.18–0.43	4.91–5.99	0.09–0.17	14.3–16.0	19.2–21.8	0.89–0.78	82.5–84.1
(web)	Opx	52.8–53.6	0.12–0.22	5.01–5.38	0.13–0.35	10.4–11.7	0.17–0.25	27.9–28.9	0.68–1.33	0.04–0.12	81.0–83.0
	Ol	39.8–40.9	0.00–0.02	0.01–0.06	0.00–0.11	15.4–16.1	0.20–0.25	41.6–43.3	0.18–0.23	0.00–0.03	82.2–83.3
Ke 782/2	Cpx	48.2–50.9	0.72–1.45	5.87–8.49	0.12–0.67	4.70–5.85	0.04–0.17	13.6–15.1	19.7–21.3	0.81–1.22	81.2–84.7
(ol-spl web)	Opx	52.8–53.9	0.18–0.28	4.26–4.80	0.22–0.32	10.2–12.0	0.09–0.27	29.0–29.8	0.7–0.93	0.03–0.10	81.4–83.8
	Ol	38.9–39.5	0.00–0.04	0.01–0.06	0.00–0.05	15.8–18.0	0.14–0.30	42.3–43.3	0.08–0.25	0.00–0.04	80.9–83.0
	Spl	0.05–0.15	0.40–0.68	52.0–55.5	6.20–9.41	18.8–21.0	0.00–0.17	16.4–17.8	0.00–0.25	n.a.	58.5–62.9
	Calcite	0.05–0.06	0.00–0.03	0.00–0.01	0.00–0.01	0.08–0.09	0.00–0.02	0.50–0.63	56.5–57.2	n.d.	92.1–92.9
Ke 1973/2	Cpx	48.4–49.0	1.02–1..30	8.75–9.21	0.03–0.15	5.41–5.84	0.09–0.14	13.4–13.8	20.5–21.4	0.88–1.16	80.8–82.8
(spl-ol	Ol (1)	39.4–39.8	0.00–0.03	0.05–0.10	0.00–0.06	15.9–16.2	0.19–0.24	42.8–44.0	0.23–0.35	0.01–0.05	82.6–83.1
cpx-ite)	Ol (2)	40.7–41.1	0.00–0.02	0.04–0.09	0.00–0.03	12.5–12.6	0.17–0.20	46.1–46.4	0.20–0.23	0.01–0.03	86.7–86.8
	Spl (1)	0.11–0.13	0.35–0.44	61.4–63.2	0.67–1.02	12.8–15.7	0.10–0.13	19.8–20.6	0.00–0.03	n.a.	67.3–72.1
	Spl (2)	0.14–0.15	0.38–0.39	56.9–58.9	5.02–6.72	14.0–14.2	0.15–0.19	19.6–20.2	0.00–0.01	n.a.	69.5–69.8

(1) ol and spl in clinopyroxenite, *(2)* ol in peridotite enclave, spl at peridotite–clinopyroxenite contact; olivine from Ke 782/2 and Ol(2) from Ke 1973/2 include 0.15–0.25 wt% NiO

[a] Including first generation (i.e., grt, cpx-I, opx-I, spl-I, ol-I, amph-i, phl, rutile and ilmenite) and second generation neoblasts (i.e., cpx-IIa and opx-IIa; *weak def.* low degree of deformation, *p. clastic* porphyroclastic fabric; note that amphiboles and phlogopite include 0.05–1.37 and 8.74–8.81 wt% K_2O, respectively; rutile in Ke 784/1 includes 0.03–0.04 wt% Nb_2O_5 and 0.04–0.05 wt% Zr_2O; olivine in Ke 1959/18 includes 0.47–0.64 NiO; Mg# = 100 × Mg/(Mg + Fe_{tot}) olivine in Ke 1960/4 includes 0.59–0.68 wt% NiO; olivine in Ke 727 and Ke 782/1 includes 0.12–0.27 wt% NiO; amphiboles include <0.79 wt% K_2O

neoblasts have compositions identical to cpx-I and opx-I rims. The same accounts for cpx-IIb and opx-IIb within symplectites (see electronic appendix A2 for representative analyses). Symplectite spinel is Cr-poor pleonast with Cr# of 0.7–6.0 [atomic Cr/(Cr + Al); Electronic Appendix A2).

Primary ol is Mg-rich (~$Fo_{86–88}$; Table 2), while NiO contents are slightly higher when compared to ol from Group I (grt)-spl lherzolites (0.47–0.68 wt% and 0.27–0.40, respectively; see Table 2 and Kaeser et al. 2006).

Pyroxene porphyroclasts and grt commonly show major element zoning: in cpx-I, total Al contents and tetrahedrally coordinated $Al^{(IV)}$ either increase (the typical case) or, more rarely, decrease from cores to rims (Fig. 4a). Ca and Na contents commonly complementarily increase and decrease from cores to rims. Consequently, the corresponding Ca* values [the temperature sensitive term Ca/(1 − Na); Brey et al. 1990] are constant (Fig. 4a). Single-grt grains show core-rim zoning characterised by decreasing Mg#, Cr# [=100 × Cr/(Cr + Al)] and TiO_2 contents, while MnO contents increase (Fig. 4b). The shape of opx-I zoning patterns depends on the adjacent phases (Fig. 4c). Grains isolated from garnet show only limited zoning, typically characterised by increasing Al concentrations from core to rim, sometimes followed again by decreasing contents towards the outermost rims (similar to opx-I from Group I xenoliths; Kaeser et al. 2006). Towards contacts with garnet, Al concentrations strongly increase (Fig. 4c). Ca profiles are either flat or slightly decrease towards rims (Fig. 4c), with few opx-I grains preserving a plateau of higher Ca contents in their core.

Volatile-bearing minerals include Cr_2O_3-poor Ti-pargasite or kaersutite and Ti-rich phlogopite (Table 2). They overlap in composition with amphibole and phlogopite from the Group I (grt)-spl lherzolites (Kaeser et al. 2006). Ilmenite is Mg-rich and contains small amounts of Al_2O_3 and Cr_2O_3 (Table 2), typical for mantle ilmenite (e.g., Kalfoun et al. 2002). Rutile contains small amounts of Cr_2O_3, Al_2O_3 and Fe_2O_3, while Nb_2O_5 and ZrO_2 contents are <0.05 wt% (Table 2).

Analyses for secondary minerals in reaction zones are given in Appendix A2. They comprise cpx_m with lower Al, Na and Ti when compared to cpx-I, ol_m with Mg# of 86.9–89.1, minor kaersutite and plagioclase. The latter ranges from oligoclase to labradorite ($Ab_{32.4–77.6}$ and $An_{22.2–67.4}$) and has low K_2O contents (<$Or_{0.3}$).

Major elements: Group VI grt-free websterites

Group VI grt-free pyroxenites contain Al-rich augite with variable TiO_2, Cr_2O_3 and Na_2O contents (Table 2; Fig. 3). Mg# correlate positively with Cr_2O_3 and negatively with TiO_2 (Fig. 3a, b). In contrast to Group V, cpx compositions overlap with those of alkaline basalt-hosted cpx megacrysts (Fig. 3). Zoning profiles (not shown) are either flat or exhibit

Table 3 Major element composition of primary inclusions in garnet of Group V grt websterite Ke 784/1 from Marsabit

Mineral	parg	parg	parg	cpx	opx
Nr.[a]	1	4	6	2	3
SiO_2	43.05	42.36	42.38	51.22	54.64
TiO_2	4.01	4.32	3.81	1.60	0.16
Al_2O_3	14.09	14.75	14.64	7.98	3.71
Cr_2O_3	0.43	0.47	0.43	0.34	0.13
$FeO_{(tot)}$	5.53	5.66	5.62	3.14	9.55
MnO	0.03	0.01	0.04	0.04	0.07
NiO	0.11	0.09	0.06	0.05	0.04
MgO	15.88	15.49	15.61	13.05	30.89
CaO	10.22	10.22	10.15	19.71	0.40
Na_2O	3.92	4.03	4.09	2.60	0.07
K_2O	0.02	n.d.	0.01	n.d.	0.01
H_2O[b]	2.10	2.09	2.08	–	–
Total	99.40	99.49	98.91	99.70	99.66
Stoich.[c]	23O	23O	23O	6O	6O
Si	6.160	6.067	6.101	1.861	1.919
Ti	0.432	0.465	0.412	0.044	0.004
Al	2.377	2.489	2.484	0.342	0.153
Cr	0.049	0.053	0.049	0.010	0.004
Fe^{2+}	0.662	0.678	0.676	0.095	0.280
Mn	0.003	0.001	0.004	0.001	0.002
Ni	0.013	0.011	0.006	0.001	0.001
Mg	3.387	3.306	3.349	0.707	1.617
Ca	1.567	1.568	1.565	0.767	0.015
Na	1.087	1.117	1.143	0.183	0.005
K	0.004	–	0.002	–	0.001
H	2.000	2.000	2.000	–	–
Total[d]	15.741	15.756	15.792	4.011	4.001
Mg#	83.7	83.0	83.2	88.1	85.2

parg Ti-pargasite, *n.d.* not detected

[a] See Fig. 1f for point localisation; [b]calculated on the basis of 2 OH per formula unit; [c]stoichiometry (calculated on the basis of *n* oxygens); [d]without H

slightly decreasing Al and increasing Ca contents towards rims. Orthopyroxene is Al-rich enstatite and bronzite ($En_{79.7–82.2}$; Table 2) with elevated TiO_2 and CaO concentrations when compared to Group V grt websterites. Olivine is $Fo_{80.1–83.3}$ and has lower NiO contents than peridotitic ol (0.05–0.27 wt%; Table 2). Spinel is pleonast with hercynite contents between 0.20–0.35 mol% and low Cr# (<10).

Trace elements

The trace element composition of Groups V and VI cpx is illustrated in Fig. 5a–h. Strongly incompatible trace element signatures of cpx from Group V samples Ke 784/1 and 1960/4 are strikingly similar to those of Group I (grt)-spl lherzolites (Fig. 5a, b, e–f). Further, sample Ke 1960/4 shows a similar HREE variation as observed in Group I samples, i.e., higher HREE-concentrations towards cpx-I rims and in cpx-IIa cores (Fig. 5f). The more incompatible REEs are progressively depleted (from Eu to La). Extended trace element plots show negative inflections for Nb, Ta, and Pb, and very weak negative Zr–Hf–Ti anomalies. Cpx-I from the opx-rich sample Ke 1959/18 has slightly higher incompatible element abundances (i.e., MREE, LREE, U and Th; Fig. 5c). Clinopyroxene from the weakly deformed spl-ol clinopyroxenite Ke 782/2 shows convex upward REE patterns and is enriched in MREE and LREE when compared to Group V. A few grains show high U–Th contents and positive deflection for La and Ce (Fig. 5h).

Trace element patterns for grt are illustrated in Fig. 6 and show that grt is the major host for the HREE (with almost flat patterns from Dy to Lu), whereas LILE, LREE and Sr are depleted (Fig. 6a, b).

Amphiboles have low HREE and variable LILE contents (Fig. 7; Table 4). REE patterns are parallel to those of the associated cpx. Sample Ke 1960/4 contains Ti-pargasite compositionally identical to that in Group I (grt)-spl lherzolites (Fig. 7). Phlogopite is the major repository for Cs, Rb and Ba and has similar trace element characteristics as phlogopite in the Group I xenoliths (Table 4; Kaeser et al. 2006). Trace element composition of opx is given in Table 4. Patterns (not shown) are characterised by low REE concentrations and positive excursions for Pb, Zr, Hf, and Ti. Trace element concentrations in Group VI olivine and spinel are low, except for Li, transition metals, Zr and Nb (see Electronic Appendix A2).

Discussion

Microstructures and mineral compositions suggest that Groups V and VI pyroxenites have distinct origins. They will thus be discussed separately. The microstructures of Group V grt websterites indicate sub-solidus deformation and mineral reactions. As we will show in the following, these features can be explained in the context of the rifting-related evolution of the mantle beneath Marsabit. Sub-solidus processes strongly obliterate earlier signatures (i.e., related to magmatic pyroxenite emplacement) and therefore need to be discussed first. The emplacement of the pyroxenites will be subsequently discussed. Finally, the origin of the Group VI grt-free pyroxenites will be addressed.

Sub-solidus *P–T* evolution of grt websterites and their relation with peridotite xenoliths

In our earlier study (Kaeser et al. 2006), we concluded that the porphyroclastic peridotite xenoliths essentially reflect pervasive deformation associated with decompression and

Table 4 Representative trace element composition (μg/g) of minerals in pyroxenites from Marsabit

Group	Group V grt websterite							Group VI
Mineral position	grt Core	cpx-I Core	cpx-I Core	cpx-IIa Core	amph	amph	phl	cpx-I Core
Sample	784/1	784/1	1959/18	1960/4	784/1	1959/15	784/1	782/2
Li	0.60	3.27	2.46	1.72	1.74	0.75	3.52	1.56
P	182	53.5	80.3	21.7	181	285	23.6	33.1
K	1.01	1.20	0.95	3.03	132	2185	84838	3.83
Sc	58.9	27.9	25.3	37.5	27.9	24.4	1.58	60.5
Ti	1,197	3,281	3,622	2,022	27,703	19,349	38,177	5,912
V	122	386	310	414	409	313	389	349
Ni	29.8	263	319	230	829	735	2,127	189
Zn	21.6	13.4	8.04	2.68	43.2	6.54	76.8	15.3
Ga	9.92	12.0	11.9	7.63	17.7	4.39	23.6	9.10
Rb	<0.009	<0.006	<0.007	<0.005	0.036	0.64	89.9	0.012
Sr	0.40	107	125	48.2	335	244	94.0	65.4
Y	23.9	4.50	8.99	6.57	8.39	15.2	0.055	10.9
Zr	16.8	23.9	45.2	21.4	33.3	46.9	0.87	27.1
Nb	0.015	0.019	0.029	0.045	3.82	3.93	4.49	0.64
Cs	<0.003	<0.002	<0.002	0.002	0.011	0.010	1.89	<0.002
Ba	<0.018	0.012	<0.021	0.049	0.41	39.7	205	0.046
La	0.021	0.86	3.40	0.63	1.48	3.77	0.013	2.86
Ce	0.039	3.42	11.5	2.33	5.26	12.3	<0.004	8.56
Pr	0.026	0.68	2.00	0.49	1.03	2.02	<0.002	1.44
Nd	0.31	4.31	11.1	3.04	6.72	12.2	<0.015	8.14
Sm	0.52	1.63	3.44	1.21	2.77	4.47	<0.012	2.56
Eu	0.33	0.61	1.06	0.44	1.19	1.63	0.011	0.92
Gd	1.54	1.74	2.87	1.35	2.92	4.24	<0.016	2.41
Tb	0.40	0.23	0.49	0.26	0.41	0.63	<0.002	0.45
Dy	3.48	1.15	2.31	1.48	2.15	3.44	<0.012	2.53
Ho	0.90	0.19	0.42	0.25	0.37	0.64	0.003	0.49
Er	2.78	0.34	0.75	0.63	0.61	1.29	<0.008	1.13
Tm	0.39	0.04	0.09	0.08	0.10	0.14	0.002	0.15
Yb	2.84	0.21	0.54	0.51	0.44	0.98	<0.017	0.89
Lu	0.46	0.03	0.09	0.07	0.053	0.12	<0.002	0.12
Hf	0.29	0.78	1.59	0.92	0.84	0.97	0.020	1.33
Ta	<0.002	0.008	0.005	<0.001	0.30	0.20	0.18	0.067
Pb	0.045	0.16	0.51	0.095	0.62	1.77	0.68	0.26
Th	<0.003	0.021	0.13	0.012	0.016	0.092	<0.004	0.18
U	0.004	0.014	0.039	0.008	0.010	0.037	0.009	0.050

The complete data set is provided in the Electronic Appendix A2

cooling in the context of multiple rifting episodes to which the lithospheric mantle in this region was subjected (Anza Graben and Kenya rift; e.g., Winn et al. 1993; Morley et al. 2006). Thermobarometric data were interpreted in terms of a *P–T* path characterised by three successive stages (Fig. 8): an early high-*P*/high–*T* stage (H*P*/H*T*: 970–1,080°C at 2.3–2.9 GPa) in the grt stability field, followed by the transition to a medium-*T* stage (M*T*: 800–900°C) and a low-*T* stage (L*T*: ~ 750–800°C), both in the spl stability field ($P < 1.5$ GPa; see Kaeser et al. 2006 for details).

Most of the microstructural and chemical features of the Group V grt websterites can be reconciled with the above defined *P–T* path. Spl–opx–cpx symplectites reflect the transition from the grt to the spl stability field, which is certainly the result of decompression. The alternative, grt–spl transition by isobaric heating, can be excluded as neither increasing Ca in pyroxene rims nor Mg# in garnet rims

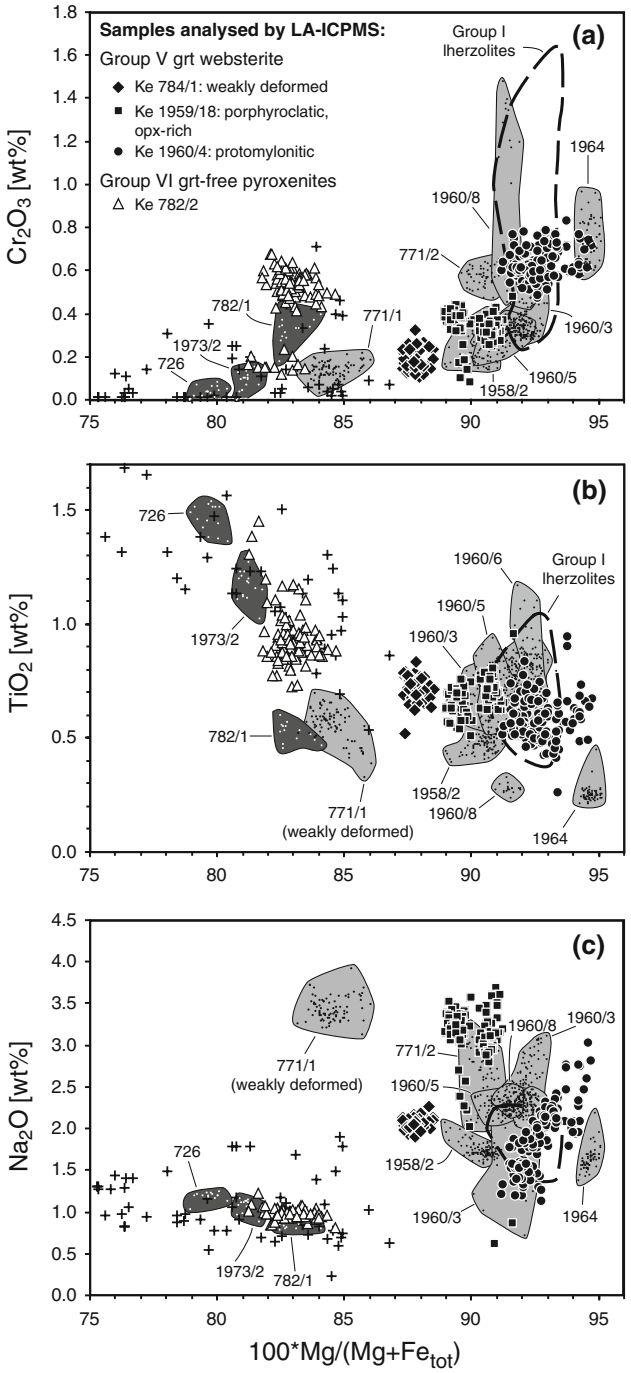

Fig. 3 Compositional variation of clinopyroxene in pyroxenite xenoliths from Marsabit. *Light-grey fields* are Group V grt websterites, *dark-grey fields* are Group VI grt-free pyroxenites (sample numbers are annotated). Samples analysed for trace elements (LA-ICP-MS) are indicated by larger symbols. *Dashed line* outlines compositional range of clinopyroxene from Group I porphyroclastic (grt)-spl lherzolites (Kaeser et al. 2006). *Crosses* indicate compositions of alkaline basalt/basanite-hosted megacryst and cumulate cpx (Righter and Carmichael 1993; Shaw and Eyzaguirre 2000; Downes et al. 2004)

point to a heating event (Fig. 4). Increasing Al concentrations (from cores to rims) in opx-I and cpx-I (Fig. 4a, c) are in agreement with decompression.

Grt-breakdown also explains elevated HREE abundances in cpx-I rims and cpx-IIa neoblasts in some samples as compared to cpx-I cores (Fig. 5f). $D_{grt/cpx}$ for HREE and Sc still correspond to values similar to equilibrium partition coefficients derived from experiments and from equilibrated natural garnet pyroxenite (see caption of Fig. 9 for references). Comparable HREE partitioning is also found in natural grt lherzolite, but the range of $D^{HREE}_{grt/cpx}$ can be much larger compared to grt pyroxenites (Fig. 9), interpreted by REE fractionation during differential sub-solidus grt growth (spl–grt transition) as a function of small-scale variations in bulk rock composition of mantle peridotite (Ionov 2004; Ionov et al. 2005). In contrast to the HREE and Sc, most of the more strongly incompatible elements (e.g., Zr, Hf, LREEs, Sr) in Group V grt websterites exhibit re-partitioning into cpx. As noted by O'Reilly and Griffin (1995), some of these features may be explained by cooling (decreasing $D^{Zr}_{grt/cpx}$) and decompression (decreasing $D^{Ti}_{grt/cpx}$).

Cooling is clearly indicated by exsolution lamellae in cpx-I and by core-rim zoning patterns such as decreasing Al in opx and cpx, present in some samples (Fig. 4a, c), by decreasing Ca contents in opx (Fig. 4c) and decreasing Mg# in grt (Fig. 4b). Slightly increasing (opx) and decreasing (cpx) Ca concentrations towards rims of the polygonal exsolution-free pyroxenes in the granular recrystallised sample Ke 1958/2 (not shown) point to later heating, similar to that recorded by the recrystallised and metasomatised Group II (grt)-spl lherzolites (Kaeser et al. 2006).

Quantitative constraints on the *P–T* evolution were obtained with the same approach as outlined in detail by Kaeser et al. (2006), based on careful evaluation of mineral zoning and thermobarometric calculations. The results are summarised below, while the interested reader is referred to Olker (2001) and the Electronic Appendix A3, where a detailed discussion of the thermobarometric calculations is provided.

The *P–T* conditions recorded in the Group V grt websterites were estimated using a combination of Brey and Köhler's (1990) grt-opx thermometer (based on Mg–Fe partitioning) and the grt–opx barometer (based on the Al solubilty in opx in the presence of grt). Application of this thermobarometer to opx-I and grt core compositions constrains the H*P*/H*T* stage to ~970–1,100°C at ~2.3–2.6 GPa, which is in excellent agreement with the *P–T* data obtained for the Group I (grt)-spl lherzolites (Fig. 8, Table 1).

Using the composition of porphyroclast rims and/or neoblast cores yields lower *P–T* conditions of ~700–800°C at ~0.5–1.0 GPa (Fig. 8, Table 1). The exception is the granular recrystallised sample Ke 1958/2 whose mineral rims record a heating event (>1,000°C; Table 1). Chromium contents in symplectitic spl-IIb constrain the maximum pressure after the grt-spl transition to <1.5 GPa (Carroll Webb and Wood 1986; Table 1), in agreement with the experimentally derived pressure for the grt–spl

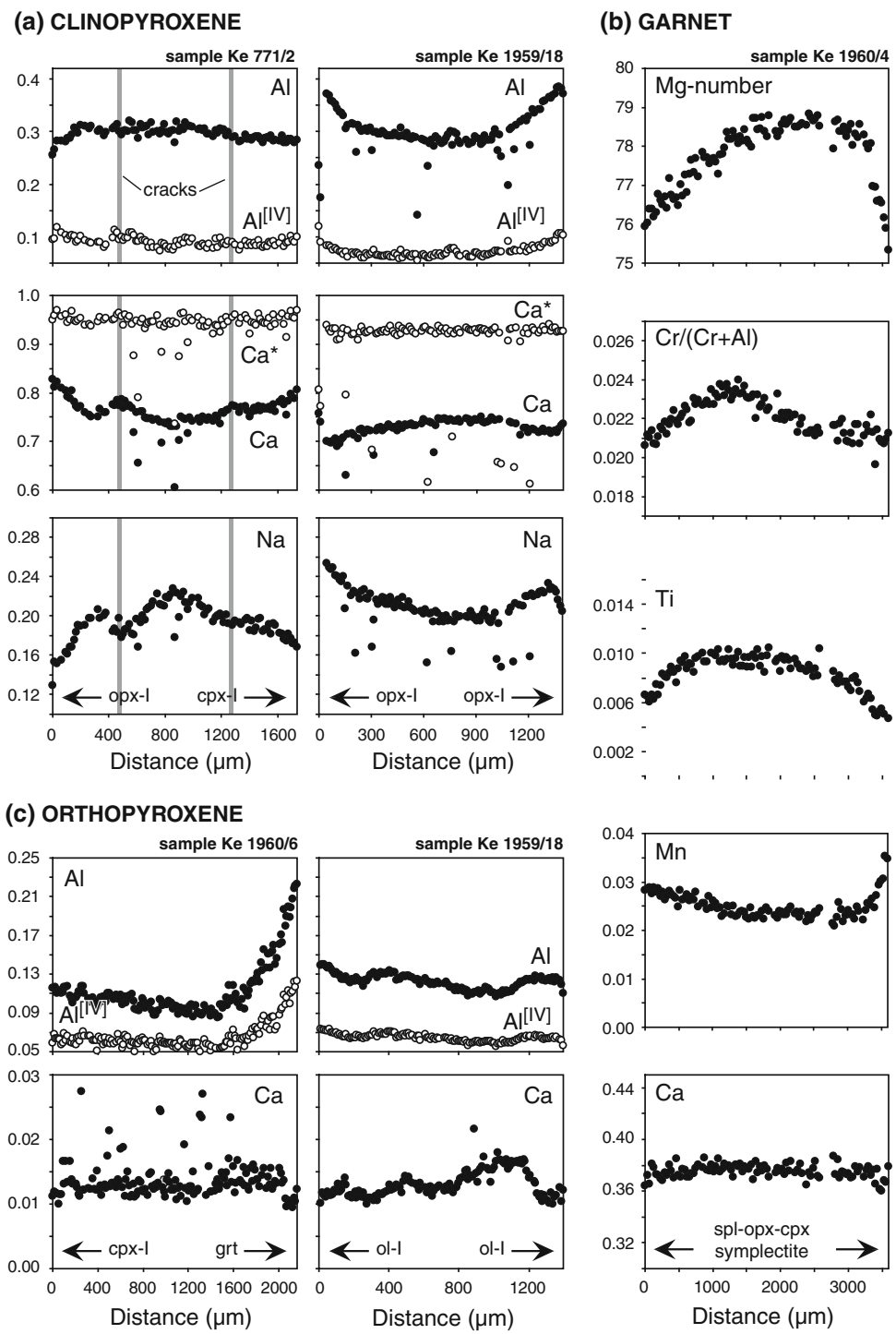

Fig. 4 Examples of major element zoning in clinopyroxene (**a**), garnet (**b**) and orthopyroxene (**c**) porphyroclasts (rim–core–rim electron microprobe traverses; *y*-axis units = cations per formula unit). Ca* = Ca/(1 − Na); Al[IV] = calculated tetrahedrally coordinated Al. Outliers in pyroxene profiles are mixed analyses (host pyroxene with cpx or opx exsolution lamellae). *Arrows* indicate adjacent phases

transition in mafic systems (1.3–1.7 GPa; Irving 1974a; Hirschmann and Stolper 1996). Pressures derived from grt and opx rims are mostly <1.0 GPa. They are in accordance with plagioclase replacing and/or co-existing with spinel in reaction zones which implies pressures of ≤0.9 GPa (Irving 1974a). However, some very low pressures estimates imply depths that are too shallow for a mantle origin (e.g. sample Ke 1960/4; see Table 1). These values either indicate disequilibrium between grt and opx or reflect the decompression of the xenoliths during their ascent to the surface. Such late-stage formation would also account for the very fine-grained nature of kelyphites and reaction zones growing at the expense of all mineral generations (porphyroclasts, neoblasts and symplectite assemblages).

The *P–T* evolution recorded by the Group V grt websterites and the Group I (grt)-spl lherzolites is very similar

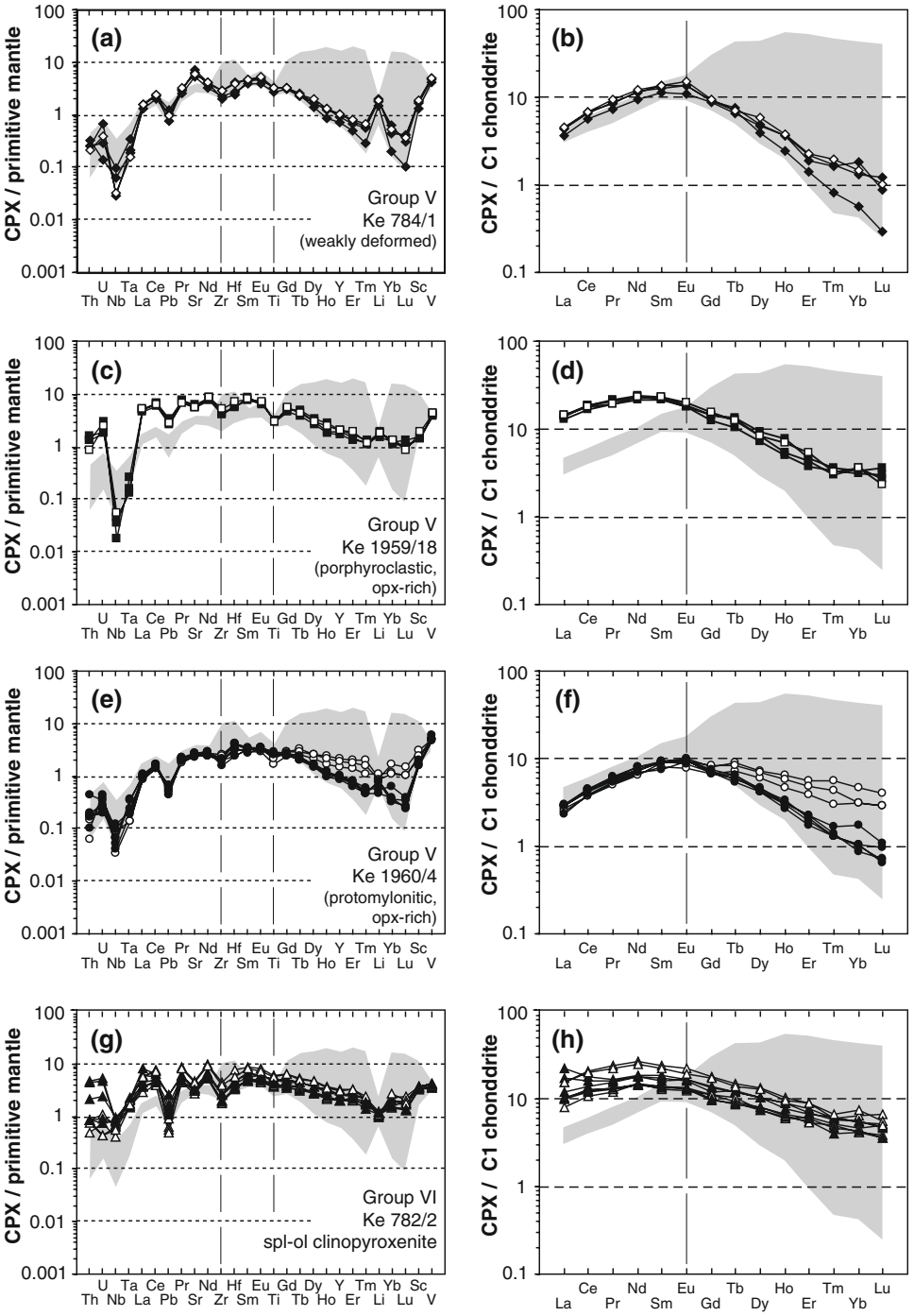

Fig. 5 Trace element composition of clinopyroxene in Marsabit pyroxenite xenoliths: **a**, **b** weakly deformed grt websterite Ke 784/1; **c**, **d** opx-rich grt websterite Ke 1959/18; **e**, **f** protomylonitic opx-rich grt websterite Ke 1960/4; **g**, **h** Group VI grt-free spl-ol clinopyroxenite Ke 782/2. *Filled symbols* are porphyroclast cores (cpx-I), *empty symbols* are either rims of porphyroclasts or cores of neoblasts (cpx-IIa). The *grey-shaded field* outlines the clinopyroxene composition of Group I (grt)-spl lherzolite xenoliths (Kaeser et al. 2006). Normalising values are from McDonough and Sun (1995)

(Fig. 8), which supports our earlier hypothesis of a close spatial relation of in the mantle prior to eruption to the surface (Kaeser et al. 2006).

Interpretation of the *P–T* evolution

The H*P*/H*T* stage possibly reflects the *P–T* conditions of a former equilibrated pyroxenite-bearing subcontinental mantle, similar to present-day thermal conditions observed in southern parts of Kenya (e.g., Chyulu), where rifting-induced lithospheric thinning is much less advanced than beneath the Anza Graben (Henjes-Kunst and Altherr 1992). Lower *P–T* conditions recorded by porphyroclast rims, neoblasts and grt-breakdown products (symplectites) in Group V grt websterites indicate cooling and decompression. Since the deformed peridotite xenoliths show a very similar *P–T* evolution (Fig. 8: the M*T* and L*T* stages; Kaeser et al. 2006), we interpret this by thinning of

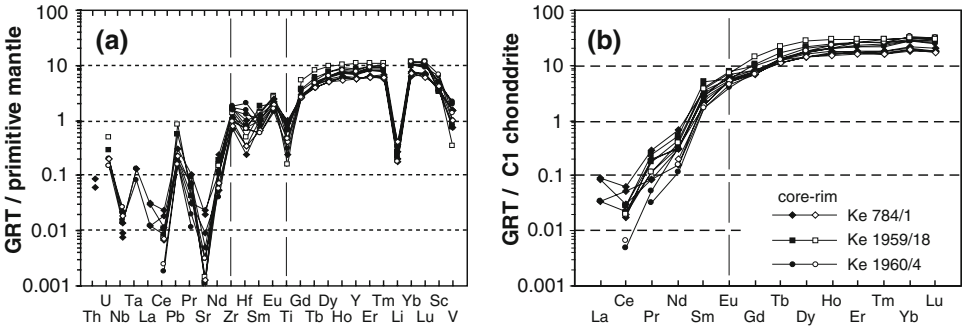

Fig. 6 Trace element composition of garnet from Group V grt websterites. Extended trace element patterns (**a**) are normalised to the primitive mantle and REE patterns (**b**) are normalised to C1 chondrite (normalising values from McDonough and Sun 1995)

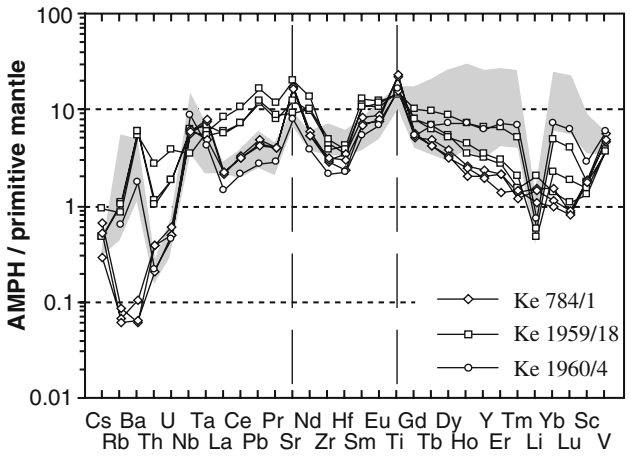

Fig. 7 Trace element patterns of amphibole in Group V grt websterite xenoliths. The *grey-shaded field* correspond to amphiboles in Group I (grt)-spl lherzolites (Kaeser et al. 2006). Normalising values (primitive mantle) from McDonough and Sun (1995)

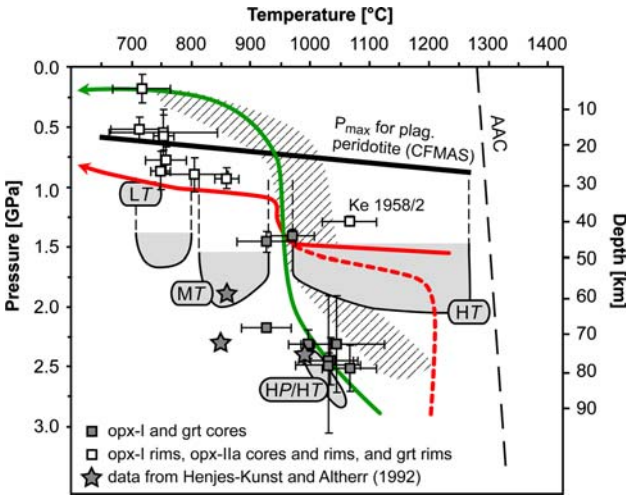

Fig. 8 Pressure–temperature stages preserved by Group V grt websterites (based on orthopyroxene-garnet thermobarometry (Brey and Köhler 1990). The results are in good agreement with the temperature estimates for the H*P*/H*T*, M*T* and L*T* stages based on Marsabit peridotite xenoliths (Kaeser et al. 2006) and further constrain their depth range. Also indicated for comparison are *P–T* evolution paths for three mantle rock massifs which have been exhumed during continental rifting: Malenco [*red*; Müntener (1997); *dashed line* peridotite; *continuous line* grt clinopyroxenite intrusion]; Ligurian grt clinopyroxenites and peridotites [*green* Montanini et al. (2006)]; Zabargad, former garnet-bearing websterites and spl peridotites [hachured field; Piccardo et al. (1988)]. Sample Ke 1958/2 represents the single-granular recrystallised and re-heated grt websterite. See text for further discussion

pyroxenite-bearing lithospheric mantle accompanied by deformation, presumably in the context of continental rifting (Anza rift; Kaeser et al. 2006).

The low *P–T* estimates of the M*T* and L*T* stages further constrain the shallow (i.e., $\leq$30 km) position of deformed grt websterites and porphyroclastic peridotites prior to their entrainment in the Marsabit basanites. *P–T* conditions based on mineral rims are similar to those reported for the metamorphic high-stress deformation stage of exhumed peridotite massifs, such as Lherz (early recrystallisation at $\sim$950°C/1.2–1.5 GPa and formation of porphyroclastic and mylonitic fabrics and foliation at 0.8–1.3 GPa; Fabriès et al. 1998, 2001). Mylonitic microstructures, both in pyroxenite (Fig. 1d) and peridotite (Group IV; Kaeser et al. 2006) are in accordance with similar observations from Pyrenean massifs as well (Fabriès et al. 1998). Moreover, the deciphered *P–T* path, microstructures and compositional features of the Marsabit pyroxenites are similar to pyroxenites from ultramafic massifs exhumed during continental rifting processes, namely, from Malenco (Müntener and Hermann 1996), the Ligurides (Montanini et al. 2006), and from Zabargad (Piccardo et al. 1988; Kurat et al. 1993; Vannucci et al. 1993; see Fig. 8). This suggests that similar uplift and deformation processes took place beneath Marsabit.

In contrast, mineral rims of the granular recrystallised sample Ke 1958/2 partly re-equilibrated at higher *T* (Table 1), within the range of the H*T* stage defined by the recrystallised and metasomatised Group II lherzolite xenoliths (Fig. 8). This result is in agreement with the fabric of this sample indicating static recrystallisation, most likely in response to the young thermal modification of the Marsabit lithosphere, resulting from Kenya rift magmatism (Kaeser et al. 2006, 2007).

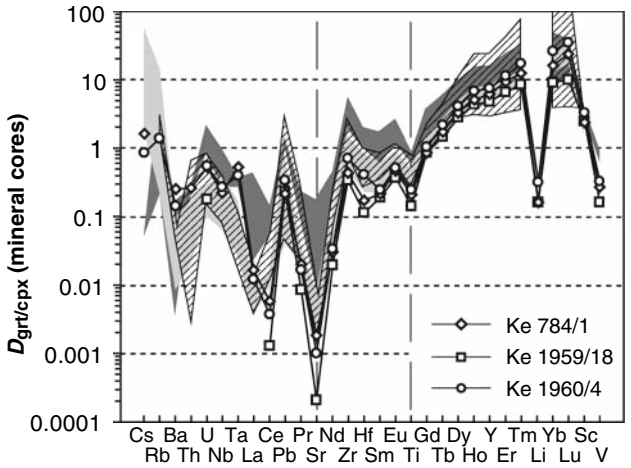

Fig. 9 Trace element partitioning between grt and cpx-I cores from Group V grt websterites from Marsabit. *Light-grey field* outlines partitioning in texturally and compositionally equilibrated natural grt pyroxenite (Bizimis et al. 2005); *dark-grey field* indicates experimentally derived grt/cpx partition coefficients (Johnson 1998; Green et al. 2000; Klemme et al. 2002; Pertermann et al. 2004); *hachured field* indicates partitioning for natural grt lherzolite xenoliths from Siberia and Mongolia for comparison (Ionov 2004; Ionov et al. 2005). For discussion see text

Peridotite-pyroxenite mingling: the result of pyroxenite emplacement and/or sub-solidus reactions?

Thermobarometry (see above) gave evidence that porphyroclastic peridotites and grt websterites experienced a closely comparable *P–T*-deformation history. In addition, the compositional data clearly revealed that increasingly deformed pyroxenite xenoliths show increasing compositional overlaps with the Group I (grt)-spl lherzolites (e.g., Figs. 3, 5, 7), implying a chemical interaction between peridotite and pyroxenite, e.g., through sub-solidus deformation-induced mingling (Kaeser et al. 2006). However, as we will show in the following, the well-preserved microstructures in the Marsabit grt websterites and compositional features indicate that peridotite-pyroxenite interaction most likely occurred during two stages: first during melt–wall-rock reaction in the context of pyroxenite intrusion, and second, during later sub-solidus deformation and re-equilibration in the context of continental rifting. Sub-solidus modification is more evident in the present case and will thus be discussed first.

A close relation between deformation and metamorphism (i.e., the grt-spl transition) is indicated microstructurally: strongly deformed grt websterites contain much more symplectite, while in the weakly deformed samples symplectite is almost absent (Fig. 1a–e). This suggests a close link between the increasing strain rate and the mineral reaction rate. However, grt-breakdown also depends on the microstructural position of the grt crystal. This is highlighted by the fact that symplectite preferentially developed in zones that are now enriched in opx, while commonly no reaction is visible at grt-cpx interfaces (Fig. 1c, e). The reason for this may be the original association of opx with ol, and the availability of ol to drive the reaction grt + ol = opx + cpx + spl. Preservation of ol-I is restricted to orthopyroxenitic domains (Fig. 1e), where, in turn, grt is commonly completely transformed to symplectite. The same was systematically observed in the Group I lherzolites, where no grt was preserved (Kaeser et al. 2006). If we assume that less opx-rich pyroxenites also contained less olivine, then the latter will be exhausted before all grt reacted to form symplectite.

Besides the availability of ol, grt-breakdown also depends on the *P–T* conditions and the bulk chemical composition. With respect to the bulk composition, adding peridotite to pyroxenite would shift the grt-spl transition to higher pressures, given the Cr-rich nature of peridotite when compared to pyroxenite (e.g., Klemme and O'Neill 2000).

All the above observations are principally in agreement with deformation-induced sub-solidus mingling and chemical re-equilibration between pyroxenite and peridotite. In addition, field observations from different exhumed mantle rock sections, where peridotite-pyroxenite relationships are better visible than in xenoliths, support such a model (e.g. Kornprobst 1966; Bodinier et al. 1987, 1988; Van der Wal and Vissers 1996; Tabit et al. 1997).

Experiments on the deformation behaviour of dry pyroxene and olivine aggregates (Chopra and Paterson 1981; Bystricky and Mackwell 2001) indicate that pyroxenite dykes, at *P–T* conditions relevant to the M*T* and L*T* stage (750–850°C at ~ 1.0–2.0 GPa; Fig. 8), will be stretched and probably disaggregated into a more plastically deforming ol matrix. This process would provide ol to drive to completion the grt-breakdown reaction in thin, cm-sized pyroxenitic layers (such as those preserved in Group I lherzolites; see Fig. 2a of Kaeser et al. 2006) or at the rims of larger pyroxenite bands.

The low *P–T* conditions, however, also imply that chemical re-equilibration of peridotite and pyroxenite depends strongly on the diffusivities of a given element. Fast diffusing elements such as Mg and Fe will potentially re-equilibrate also in larger porphyroclasts, even at relatively low temperatures (see discussion of the pyroxene and garnet zoning patterns). In contrast, slowly diffusing elements, such as the trivalent ions Al and Cr (e.g., Freer 1981), will preserve earlier, e.g., magmatic signatures. In this respect, higher Cr-contents in more strongly deformed websterites (e.g., Fig. 3a) more likely reflect melt-peridotite interaction (e.g., at the margin of pyroxenite layers) during pyroxenite emplacement (e.g., O'Reilly and Griffin 1987; Litasov et al. 2000) rather than diffusional Cr

addition at low temperatures. High Cr-contents coinciding with strong deformation would then simply indicate that deformation was more intense at the margins of pyroxenite dykes, which were also the site of previous melt-peridotite interaction. Melt crystallised in the centre of pyroxenite bodies, in turn, did not interact with peridotite. The resulting Al-rich and Cr-poor websterite was later protected from deformation (e.g., during boudinage). Similar models of interfering 'magmatic' and sub-solidus signatures were reported from peridotite massifs such as Lherz (Bodinier et al. 1987); Balmuccia (Rivalenti et al. 1995), Ronda (Garrido and Bodinier 1999) and Beni Bousera (Tabit et al. 1997; Kumar et al. 1996), as well as from xenoliths (Litasov et al. 2000; Liu et al. 2005).

Finally, earlier melt-peridotite reaction could also explain the presence of the opx-rich domains. Replacement of ol by opx typically occurs during interaction of peridotite and opx-saturated basaltic melt (Sen and Dunn 1995; Kelemen et al. 1998). In analogy to observations from exhumed mantle rock massifs, these opx-rich domains were presumably localised at pyroxenite–peridotite interfaces. The very Ni-rich composition of ol-I (Table 2) would be in agreement with such an origin, i.e., reflecting Ni re-partitioning from an originally olivine-rich rock into an ol-poor pyroxenitic rock, where Ni contents are no longer buffered by peridotitic olivine. It should be noted that the inverse is observed where harzburgite is transformed into dunite during melt–rock reaction processes (Suhr 1999). The high Ni contents in ol from Group V pyroxenites is in accordance with recent models that explain the formation of olivine-free reaction pyroxenites during Si-rich melt metasomatism (Sobolev et al. 2005).

Origin of the grt websterites

Minerals from Group V grt websterites are all characterised by high Mg# (Table 2). In addition, cpx shows LREE-depleted trace element patterns (Fig. 5) and grt has high HREE concentrations (Fig. 6). These features can be reconciled with an origin as crystal segregates or cumulates from basaltic melts. With respect to the geodynamic evolution of the mantle beneath Marsabit, Group V grt websterites thus most likely represent ancient 'metacumulate' rocks, crystallised from melts that formed either in a convergent setting during Pan-African times, or in the context of the later evolution of the lithosphere, characterised by multiple rifting events from the Mesozoic until present days.

From all studied xenoliths, sample Ke 784/1 shows the lowest degree of deformation and also contains the least (if any) 'peridotitic' component added during subsolidus mingling with peridotite (e.g., low Cr-content in cpx; see Fig. 3a). The microstructures, phase assemblage and mineral compositions of this sample can therefore be used to constrain the 'pre-metamorphic' origin and the compositional nature of the melt(s) parental to the Group V grt websterites. First of all, inclusions of large euhedral cpx-I in garnet point to clinopyroxene as being the earliest liquidus phase. Olivine would appear even earlier (e.g., Kogiso et al. 2004, and references therein); however, judging from the lack of ol-consuming reaction products (i.e., symplectite after grt) it can be supposed that sample Ke 784/1 contained no magmatic ol. A magmatic origin of grt is indicated by its high modal abundances and large subhedral crystal sizes (i.e., unlike grt of subsolidus exsolution origin, which commonly occurs as interstitial blebs or lamellae in pyroxene; e.g., Conquéré 1977; Ulianov and Kalt 2006). High HREE contents of grt (Fig. 6) and $D^{\mathrm{HREE}}_{\mathrm{grt/cpx}}$ values close to equilibrium partition coefficients (Fig. 9) support a magmatic origin. Crystallisation of grt from basaltic liquids is restricted to high pressure (>1.0–3.0 GPa depending on the bulk composition; see Kogiso et al. 2004 and references therein). Such conditions are in agreement with estimates for the H*P*/H*T* stage (Fig. 8).

Besides large cpx-I crystals, the cores of grt contain variable amounts of euhedral Ti-pargasite, rutile needles and rare opx. Almost all of them (except rutile) are very unlikely to have formed by sub-solidus exsolution processes. Opx exsolution, for example, would imply an earlier ultrahigh-pressure stage (majoritic garnet), for which we do not have any indication. Given the low Na_2O in upper mantle-derived garnet, amphibole exsolution is also unlikely. Therefore, we interpret both opx and amphibole as primary magmatic inclusions that crystallised contemporaneously with grt.

The origin of amphibole and opx-I outside garnet is less clear: amphibole could also have crystallised from late-stage fluids (e.g., Ho et al. 2000; Fabriès et al. 2001), while opx-I may have exsolved from earlier high-*T* cpx. However, since both minerals also occur as inclusions in grt, we prefer to interpret them as primary magmatic phases. The same probably holds true for phlogopite (Fig. 1b); neither replacement microstructures nor geochemical arguments (e.g., incompatible element enrichment in other minerals) indicate a later metasomatic origin.

Several models have been proposed to explain oriented rutile needles in garnet. In cases where rutile is associated with pyroxene it may form by subsolidus exsolution from garnet (e.g., Hwang et al. 2007, and references therein). Here, however, rutile also forms composite inclusions with Ti-pargasite (Fig. 1f). Since the latter cannot be of exsolution origin (see above), we prefer to interpret rutile as a magmatic phase, presumably formed by epitactic overgrowth during grt crystallisation, as indicated by their oriented distribution. Such a primary origin is supported by

the presence of rutile outside garnet, now mantled by ilmenite (Fig. 1g).

A consequence of the above observations is that the melt—at the time of grt crystallisation—was opx-saturated and contained about 4 wt% H_2O (to stabilise amphibole). The co-existence of rutile, Ti-pargasite and probably Ti-rich phlogopite points to Ti saturation in the initial melt ($\sim$0.5–2.0 wt% TiO_2 depending on *P*, *T*, SiO_2 and H_2O content; e.g., Xiong et al. 2005, and references therein). The solidus temperature of basaltic melts with some H_2O (i.e., H_2O-undersaturated conditions), required to account for Ti-pargasite to crystallise earlier than or contemporaneously with garnet, is about 1,000–1,100°C (at $\sim$2.0 GPa; e.g., Niida and Green 1999; Ulmer 2001, and references therein). The presence of garnet and co-existence of amphibole and phlogopite indicate high pressures, in line with crystallising depths $\geq$60 km (i.e., 2.0 GPa) in agreement with emplacement conditions in the range of the H*P*/H*T* stage ($\sim$970–1,100°C at $\sim$2.3–2.6 GPa; Fig. 8). The opx/cpx ratio during high-*P* fractionation of opx-saturated liquids (websterite crystallisation) decreases with decreasing temperature and/or increasing H_2O in the melt (Müntener et al. 2001). In their experiments, Müntener et al. (2001) found grt pyroxenite (with 4.9 wt% opx) to crystallise at 1,110°C and amph-bearing grt pyroxenite (8.8 wt% opx; 8.9 wt% amph) at 1,070°C (in both cases at 1.2 GPa with $\sim$5 wt% H_2O in the melt). Similar phase proportions and thermal conditions (but higher *P*; see Fig. 8) are obtained for the Marsabit grt websterites and define the H*P*/H*T* stage, which probably corresponds well to the *P*–*T* conditions to which the melts cooled during intrusion and crystallised the Marsabit grt websterites.

The bulk compositions of such grt-bearing H*P* cumulates have <50 wt% SiO_2, 11.4–13.6 wt% Al_2O_3 and 15.7–17.4 wt% MgO (Müntener et al. 2001). This is similar to a rough estimate of the composition of xenolith Ke 784/1 that contains, based on its mode (Table 1) and average grt, cpx and opx composition, $\sim$46–49 wt% SiO_2, $\sim$10–14 wt% Al_2O_3 and of $\sim$ 16–18 wt% MgO (range accounts for $\pm$ 10 vol% for cpx and grt contents, given the large crystal sizes, heterogeneous mineral distribution and small sample size).

Opx-saturation of melts parental to the grt websterites is in contrast to the silica-undersaturated alkaline host basalts and basanites erupted within the Marsabit volcanic complex. Hence, grt websterites most likely reflect an older magmatic modification of the lithospheric mantle, in accordance with the sub-solidus history indicating intrusion prior to rifting-related uplift and cooling. The Si-rich nature of the melts either reflects dissolution of large amounts of olivine and orthopyroxene from wall-rock peridotite by alkaline melts in deeper levels prior to crystallisation (e.g., Fabriès et al. 2001) or the intrusion of calc-alkaline or tholeiitic melts into the lithospheric mantle (i.e., in a convergent tectonic setting). The latter hypothesis suggests that a relation to an ancient, Pan-African, convergent tectonic setting is at least plausible. Further support for this hypothesis may be provided by the fact that very similar grt pyroxenites, in terms of modal compositions, whole rock and mineral chemistry, are reported from *bona fide* arc-related xenolith suites, such as the well known grt pyroxenites from the Sierra Nevada (Lee et al. 2006; and references therein). In the context of the Tertiary–Quaternary Afro-Arabian rift system, evidence for ancient (Pan-African) mantle magmatism/metasomatism in a convergent tectonic regime comes from mafic xenoliths (granulites and pyroxenites) from the Chyulu Hills, southern Kenya (Ulianov and Kalt 2006; Ulianov et al. 2006). Similar to the Chyulu Hills, the crustal basement of the Marsabit volcanic field consists of Precambrian polymetamorphic rocks of the Mozambique mobile belt resulting from multiple Pan-African accretion events (e.g., Key et al. 1989; Nyamai et al. 2003). The preservation of mantle rocks recording the same events would be a logical consequence, yet, has to be tested by further work.

Grt-free pyroxenites: cumulates from alkaline melts

Mineralogical compositions and microstructures of the Group VI pyroxenites are very similar to mafic xenoliths described from numerous intraplate alkaline magmatic settings (Wilshire and Shervais 1975; Frey 1980; Irving 1974a, b, 1980; O'Reilly and Griffin 1987). These rocks are typically interpreted in terms of high-*P* cumulates or crystal segregates from alkaline melts and may be cognate to their host lava (Irving and Frey 1984). A similar origin is indicated for Group VI pyroxenites by the trace element signature of cpx-I from xenolith Ke 782/2, which exhibits a convex-upward REE pattern, typical for clinopyroxene and amphibole megacrysts from intraplate alkaline magmas (Irving and Frey 1984, Righter and Carmichael 1993; Shaw and Eyzaguirre 2000; Downes et al. 2004). The major element characteristics of Group VI cpx are also similar to such megacryst suites (Fig. 3a–c). Trace element patterns of calculated melts in equilibrium with cpx-I of sample Ke 782/2 (using *D*-values of Adam and Green 2006) are very similar to the composition of the xenolith-hosting Quaternary Marsabit basanites (Fig. 10), suggesting that this sample probably formed during the same magmatic episode. Some cpx-I cores record slightly LREE-U-Th enriched signatures (Fig. 5g–h) which may point to the presence of small amounts of more evolved, trapped melt.

The occurrence of opx is restricted to samples characterised by sub-solidus and deformation-related

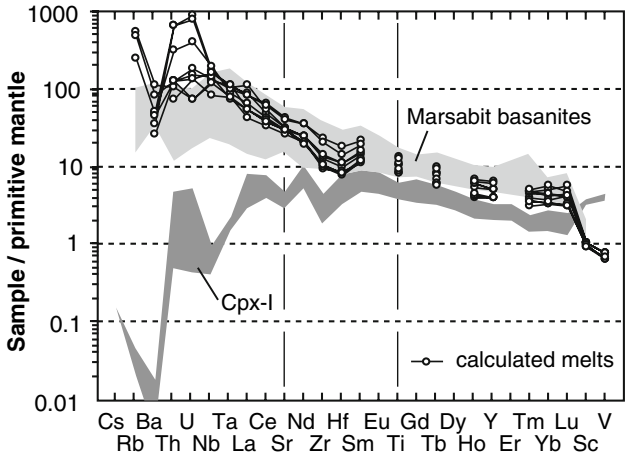

Fig. 10 Melts calculated to be in equilibrium with clinopyroxene from the Group VI spl-ol clinopyroxenite xenolith Ke 782/2. The trace element composition of Quaternary xenolith-hosting basanites from Marsabit are shown for comparison (Volker 1990). Cpx/basanite melt partition coefficients from Adam and Green (2006): run R79 (1,075°C at 1.0 GPa). Normalising values (primitive mantle) from McDonough and Sun (1995)

microstructures. Further, opx-I in sample Ke 782/2 occurs exclusively as small irregular grains in interstices between large cpx-I grains. These features point to a sub-solidus origin of opx, e.g., exsolved from cpx during cooling. This is in agreement with an alkaline parental melt crystallising at $P < 2.5$ GPa. At these conditions olivine replaces orthopyroxene as a liquidus phase (e.g., Adam 1990; Adam and Green 2006). Spinel occurs in similar microstructural positions as opx and was also observed as exsolution lamellae in sample Ke 782/2. This type of spinel is thus possibly of sub-solidus origin as well. In contrast, spinel in sample Ke 726 forms large, subhedral grains, pointing towards a magmatic origin.

The lack of feldspar and garnet confines the pressure to be between ~0.9 GPa (no plagioclase) and 1.3–1.7 GPa (no garnet; Irving 1974a; Hirschmann and Stolper 1996). These estimates are in the range of the maximum pressures (1.43–1.51 GPa; Table 1), calculated by the Cr-contents in spinels using the calibration of Carroll Webb and Wood (1986). Temperature estimates were only obtained for the sub-solidus stage using diopside-enstatite solvus thermometry (Brey and Köhler 1990) based on opx-I and cpx-I pairs. The results indicate partial re-equilibration and opx exsolution at about ~950–1,100°C (at $P_{\text{assumed}} = 1.2$ GPa; Table 1). The presence of opx and spl exsolution lamellae in cpx-I from sample Ke 782/2 indicates somewhat higher earlier temperatures (i.e., corresponding to the magmatic crystallisation). Such high temperatures, beyond the stability of Ti-rich amphibole (Niida and Green 1999), may explain the lack of amphibole in all Group VI pyroxenites. This *P–T* evolution—cooling from crystallisation temperatures to ~950–1,100°C at pressures between 0.9 and 1.7 GPa—is similar to that of other pyroxenite xenoliths entrained by intraplate alkaline magma (Wilkinson and Stolz 1997).

Of the four studied Group VI xenoliths, three show subsolidus features (opx and spl exsolution, recrystallisation and kinkbands in ol; Fig. 2a–c) indicating that they are not cognate to their host lava. The occurrence of deformed cumulates from alkaline melts can be explained by the long-time magmatic activity in the region of Marsabit, starting in Mesozoic–Paleogene times (i.e., diabase intrusion associated with the development of the Anza Graben; Winn et al. 1993; Morley et al. 2006), until the development of the Marsabit shield volcano. The xenolith-bearing basanites and alkali basalts represent the youngest volcanic products (1.8–0.5 Ma; Brotzu et al. 1984; Key et al. 1987) and thus potentially sampled mafic lithologies accumulated earlier. The presence of such material is supported by seismic studies providing evidence for presence of mafic material underplating the lowermost crust beneath the rift flanks of the Kenya rift (Mechie et al. 1997) and by the occurrence of pyroxenite xenoliths in South Ethiopian basanites interpreted to have formed during Quaternary alkaline magmatic activity (Orlando et al. 2006).

Conclusions

Microstructures and compositional features of pyroxenite xenoliths suggest two magmatic events adding mafic material to the lithospheric mantle beneath Marsabit. Pyroxenite emplacement and later modification could be summarised by three stages illustrated in Fig. 11:

1. Basaltic melts intrude the thick sub-continental lithospheric mantle (at depths > 60 km) prior to the onset of Mesozoic–Paleogene continental rifting (Anza Graben). High-pressure fractional crystallisation and melt-peridotite interaction during cooling from magmatic to ambient mantle temperatures (the H*P*/H*T* stage) resulted in a heterogeneous mantle composed of peridotite and grt websterite. Opx-saturation of the melts could suggest that they have formed in a convergent tectonic setting, i.e., during orogenesis in Pan-African times. This hypothesis needs further testing, e.g., by radiogenic isotope studies.
2. The onset of continental rifting leads to the formation of the Anza Graben and to thinning (uplift) of the lithospheric mantle. Rifting is accompanied by cooling and pervasive deformation affecting both peridotite and grt websterite. Given the rheological contrast between peridotite and pyroxenite, the latter may have undergone boudinage. Disruption of grt websterite and

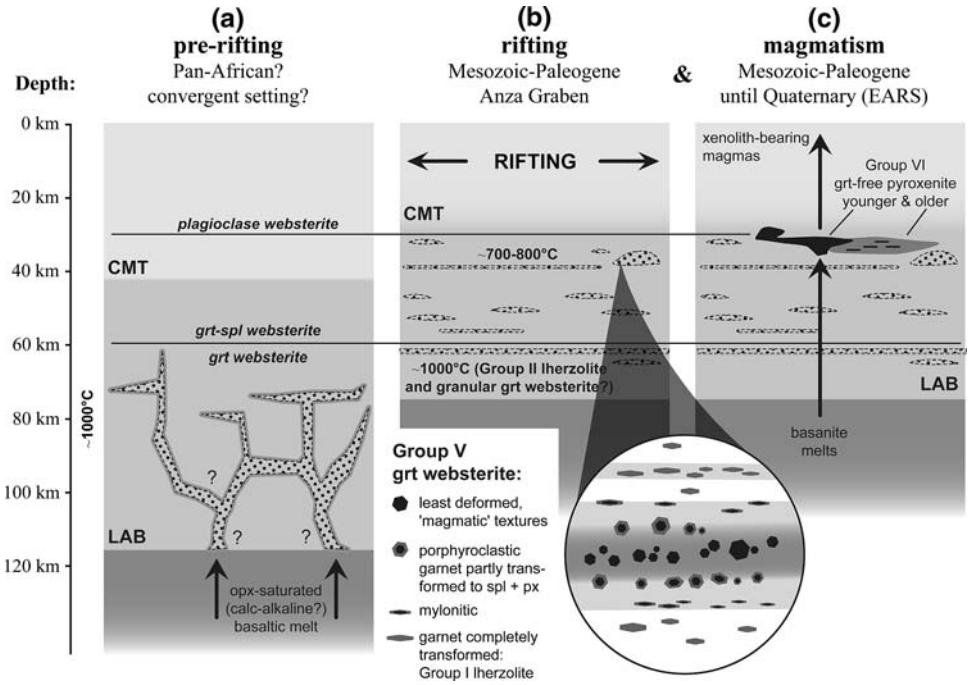

Fig. 11 Cartoon illustrating the possible petrogenesis and relationship of Groups V and VI pyroxenites: **a** crystallisation of Group V grt websterite from opx-saturated melt prior to continental rifting; **b** deformation and sub-solidus transformation of Group V grt websterite during continental rifting; **c** formation of Group VI grt-free pyroxenite during multiple intrusion of alkaline basaltic melt during Tertiary–Quaternary magmatism. *Inlet* shows the possible relation between deformation and garnet-spinel transition; LAB and CMT are 'lithosphere-asthenosphere boundary' and 'crust-mantle transition', respectively (depths from Henjes-Kunst and Altherr 1992). The pre-rift stage (**a**) corresponds to the present-day thermal stage beneath the Chyulu Hills (southern Kenya; Henjes-Kunst and Altherr 1992); Temperature estimates as in Fig. 8. Phase transitions in websterite after Hirschmann and Stolper (1996); grt-spl) and Irving (1974a; spl-plagioclase). For further explanations see text

chemical re-equilibration led to mechanical, sub-solidus mingling between peridotite and pyroxenite.

3. Multiple continental rifting was accompanied by alkaline magmatic activity (Mesozoic? until present days). Throughout this period, presumably multiple episodes of alkaline magma intrusion added further mafic material to the lithospheric mantle. Material that intruded (slightly) earlier underwent sub-solidus modification by ongoing rifting (related to the Anza Graben and/or EARS-related rifting?), whereas the youngest material escaped modification. Tertiary–Quaternary magmas finally sampled xenoliths of all types of mafic rocks and transported them to the surface.

Acknowledgments We would like to thank Ilona Fin, Oliver Wienand (Heidelberg) and André Villard (Neuchâtel) for technical assistance, as well as Hans–Peter Meyer (Heidelberg) and Edwin Gnos (Bern) for help during microprobe analyses. Constructive reviews from Cin–Ty Lee and Dmitri Ionov are greatly appreciated and helped to improve the manuscript. This study is the result of the Ph.D. theses of B·K. and B·O. were financially supported by the Swiss National Science Foundation (grant 200021–109427/1 to A.K.) and by the 'Graduiertenförderung of Land Baden–Württemberg', respectively.

References

Adam J (1990) The geochemistry and experimental petrology of sodic alkaline basalts from Oatlands, Tasmania. J Petrol 31(6):1201–1223

Adam J, Green T (2006) Trace element partitioning between mica- and amphibole-bearing garnet lherzolite and hydrous basanitic melt: 1. Experimental results and the investigation of controls on partitioning behaviour. Contrib Mineral Petrol 152(1):1–17

Allègre CJ, Turcotte DL (1986) Implications of a 2-component marble-cake mantle. Nature 323(6084):123–127

Bizimis M, Sen G, Salters VJM, Keshav S (2005) Hf–Nd–Sr isotope systematics of garnet pyroxenites from Salt Lake Crater, Oahu, Hawaii: evidence for a depleted component in Hawaiian volcanism. Geochim Cosmochim Acta 69(10):2629–2646

Bodinier JL, Dupuy C, Dostal J (1988) Geochemistry and petrogenesis of eastern Pyrenean peridotites. Geochim Cosmochim Acta 52(12):2893–2907

Bodinier JL, Godard M (2003) Orogenic, ophiolitic, and abyssal peridotites. In: Holland HD, Turrekian KK (eds) Treatise on geochemistry, vol 2. Elsevier, Amsterdam, pp 103–170

Bodinier JL, Guiraud M, Fabries J, Dostal J, Dupuy C (1987) Petrogenesis of layered pyroxenites from the Lherz, Freychinede and Prades ultramafic bodies (Ariège, French Pyrenees). Geochim Cosmochim Acta 51(2):279–290

Brey GP, Köhler T (1990) Geothermobarometry in four-phase lherzolites: II. New thermobarometers, and practical assessment of existing thermobarometers. J Petrol 31(6):1353–1378

Brey GP, Köhler T, Nickel KG (1990) Geothermobarometry in four-phase lherzolites: I. Experimental results from 10 to 60 kb. J Petrol 31(6):1313–1352

Brotzu P, Morbideli L, Nicoletti M, Piccirillo EM, Traversa G (1984) Miocene to quaternary volcanism in eastern Africa: sequence and chronology. Tectonophys 101:75–86

Bystricky M, Mackwell S (2001) Creep of dry clinopyroxene aggregates. J Geophys Res 106(B7):13443–13454

Carroll Webb SA, Wood BJ (1986) Spinel–pyroxene–garnet relationship and their dependence on Cr/Al ratio. Contrib Mineral Petrol 92:471–480

Chopra PN, Paterson MS (1981) The experimental deformation of dunite. Tectonophys 78(1–4):453–473

Conquéré F (1977) Pétrologie des pyroxènites litées dans les complexes ultramafiques de l'Ariège (France) et autres gisements de lherzolite à spinelle. Compositions minéralogiques et chimiques, évolution des conditions d'équilibre des pyroxénites. Bull Soc Fr Mineral Crystallogr 100(1):42–80

Downes H (2007) Origin and significance of spinel and garnet pyroxenites in the shallow lithospheric mantle: ultramafic massifs and orogenic belts in western Europe and NW Africa. Lithos in press: doi:10.1016/j.lithos.2007.05.006

Downes H, Beard A, Hinton R (2004) Natural experimental charges: an ion-microprobe study of trace element distribution coefficients in glass-rich hornblendite and clinopyroxenite xenoliths. Lithos 75(1–2):1–17

Fabriès J, Lorand JP, Bodinier JL (1998) Petrogenetic evolution of orogenic lherzolite massifs in the central and western Pyrenees. Tectonophys 292(1–2):145–167

Fabriès J, Lorand JP, Guiraud M (2001) Petrogenesis of the amphibole-rich veins from the Lherz orogenic Iherzolite massif (Eastern Pyrenees, France): a case study for the origin of orthopyroxene-bearing amphibole pyroxenites in the lithospheric mantle. Contrib Mineral Petrol 140(4):383–403

Freer R (1981) Diffusion in silicate minerals and glasses: a data digest and guide to the literature. Contrib Mineral Petrol 76(4):440–454

Frey FA (1980) The origin of pyroxenites and garnet pyroxenites from Salt-Lake Crater, Oahu, Hawaii: trace-element evidence. Am J Sci 280:427–449

Garrido CJ, Bodinier JL (1999) Diversity of mafic rocks in the Ronda peridotite: evidence for pervasive melt-rock reaction during heating of subcontinental lithosphere by upwelling asthenosphere. J Petrol 40(5):729–754

Green TH, Blundy JD, Adam J, Yaxley GM (2000) SIMS determination of trace element partition coefficients between garnet, clinopyroxene and hydrous basaltic liquids at 2–7.5 GPa and 1080–1200°C. Lithos 53(3–4):165–187

Henjes-Kunst F, Altherr R (1992) Metamorphic petrology of xenoliths from Kenya and northern Tanzania and implications for geotherms and lithospheric structures. J Petrol 33(5):1125–1156

Hirschmann MM, Stolper EM (1996) A possible role for garnet pyroxenite in the origin of the ''garnet signature'' in MORB. Contrib Mineral Petrol 124(2):185–208

Ho KS, Chen JC, Smith AD, Juang WS (2000) Petrogenesis of two groups of pyroxenite from Tungchihsu, Penghu Islands, Taiwan Strait: implications for mantle metasomatism beneath SE China. Chem Geol 167(3–4):355–372

Hwang SL, Yui TF, Chu HT, Shen P, Schertl HP, Zhang RY, Liou JG (2007) On the origin of oriented rutile needles in garnet from UHP eclogites. J Metam Geol 25(3):349–362

Ionov D (2004) Chemical variations in peridotite xenoliths from Vitim, Siberia: inferences for REE and Hf behaviour in the garnet-facies upper mantle. J Petrol 45(2):343–367

Ionov DA, Blichert-Toft J, Weis D (2005) Hf isotope compositions and HREE variations in off-craton garnet and spinel peridotite xenoliths from central Asia. Geochim Cosmochim Acta 69(9):2399–2418

Irving AJ (1974a) Geochemical and high-pressure experimental studies of garnet pyroxenite and pyroxene granulite xenoliths from the delegate basaltic pipes, Australia. J Petrol 15(1):1–40

Irving AJ (1974b) Pyroxene-rich ultramafic xenoliths in the Newer Basalts of Victoria, Australia. Neues Jahrb Mineral 120:147–167

Irving AJ (1980) Petrology and geochemistry of composite ultramafic xenoliths in alkalic basalts and implifications for magmatic processes within the mantle. Am J Sci 280:389–426

Irving AJ, Frey FA (1984) Trace-element abundances in megacrysts and their host basalts: constraints on partition coefficients and megacryst genesis. Geochim Cosmochim Acta 48(6):1201–1221

Johnson KTM (1998) Experimental determination of partition coefficients for rare earth and high-field-strength elements between clinopyroxene, garnet, and basaltic melt at high pressures. Contrib Mineral Petrol 133(1–2):60–68

Kaeser B, Kalt A, Pettke T (2006) Evolution of the lithopsheric mantle beneath the Marsabit volcanic field (northern Kenya): constraints from microstructural, *P–T* and geochemical studies on xenoliths. J Petrol 47(11):2149–2184

Kaeser B, Kalt A, Pettke T (2007) Crystallisation and breakdown of metasomatic phases in graphite-bearing peridotite xenoliths from Marsabit (Kenya). J Petrol 48:1725–1760

Kalfoun F, Ionov D, Merlet C (2002) HFSE residence and Nb/Ta ratios in metasomatised, rutile-bearing mantle peridotites. Earth Planet Sci Lett 199:49–65

Kelemen PB, Hart SR, Bernstein S (1998) Silica enrichment in the continental upper mantle via melt/rock reaction. Earth Planet Sci Lett 164(1–2):387–406

Key RM, Rop BP, Rundle CC (1987) The development of the late Cenozoic alkali basaltic Marsabit shield volcano, northern Kenya. J Afr Earth Sci 6:475–491

Key RM, Charsley TJ, Hackman BD, Wilkinson AF, Rundle CC (1989) Superimposed upper Proterozoic collision-controlled orogenies in the Mozambique orogenic belt of Kenya. Precambr Res 44(3–4):197–225

Klemme S, O'Neill HS (2000) The near-solidus transition from garnet lherzolite to spinel lherzolite. Contrib Mineral Petrol 138:237–248

Klemme S, Blundy JD, Wood BJ (2002) Experimental constraints on major and trace element partitioning during partial melting of eclogite. Geochim Cosmochim Acta 66(17):3109–3123

Kogiso T, Hirschmann MM, Pertermann M (2004) High-pressure partial melting of mafic lithologies in the mantle. J Petrol 45(12):2407–2422

Kopylova MG, O'Reilly SY, Genshaft YS (1995) Thermal state of the lithosphere beneath Central Mongolia: evidence from deep-seated xenoliths from the Shavaryn-Saram volcanic centre in the Tariat depression, Hangai, Mongolia. Lithos 36(3–4):243–255

Kornprobst J (1966) A propos des peridotites du massif des Beni-Bouchera (Rif septentrional Maroc). Bull Soc Fr Mineral Crystallogr 89(3):399–404

Kornprobst J, Piboule M, Roden M, Tabit A (1990) Corundum-bearing garnet clinopyroxenites at Beni Bousera (Morocco): original plagioclase-rich gabbros recrystallized at depth within the mantle. J Petrol 31(3):717–745

Kumar N, Reisberg L, Zindler A (1996) A major and trace element and strontium, neodymium, and osmium isotopic study of a thick pyroxenite layer from the Beni Bousera ultramafic complex of northern Morocco. Geochim Cosmochim Acta 60(8):1429–1444

Kurat G, Palme H, Embeyisztin A, Touret J, Ntaflos T, Spettel B, Brandstatter F, Palme C, Dreibus G, Prinz M (1993) Petrology and geochemistry of peridotites and associated vein rocks of Zabargad-Island, Red-Sea, Egypt. Mineral Petrol 48(2–4):309–341

Lee CTA, Cheng X, Horodyskyj U (2006) The development and refinement of continental arcs by primary basaltic magmatism,

garnet pyroxenite accumulation, basaltic recharge and delamination: insights from the Sierra Nevada, California. Contrib Mineral Petrol 151(2):222–242

Litasov KD, Foley SF, Litasov YD (2000) Magmatic modification and metasomatism of the subcontinental mantle beneath Vitim volcanic field (East Siberia): evidence from trace element data on pyroxenite and peridotite xenoliths from miocene picrobasalt. Lithos 54:83–114

Liu YS, Gao S, Lee CTA, Hu SH, Liu XM, Yuan HL (2005) Melt-peridotite interactions: links between garnet pyroxenite and high-Mg# signature of continental crust. Earth Planet Sci Lett 234(1–2):39–57

McDonough WF, Sun SS (1995) The composition of the Earth. Chem Geol 120:223–253

Mechie J, Keller GR, Prodehl C, Khan MA, Gaciri SJ (1997) A model for the structure, composition and evolution of the Kenya rift. Tectonophys 278:95–119

Montanini A, Tribuzio R, Anczkiewicz R (2006) Exhumation history of a garnet pyroxenite-bearing mantle section from a continent-ocean transition (northern Apennine ophiolites, Italy). J Petrol 47:1943–1971

Morley CK, Day RA, Lauck R, Bosher R, Stone DM, Wigger ST, Wescott WA, Haun D, Bassett N, Bosworth W (2006) Geology and geophysics of the Anza Graben. In: Morley CK (ed) Geoscience of rift systems: evolution of East Africa, vol 44. AAPG studies in geology, Tulsa, pp 67–90

Müntener O (1997) The Malenco peridotites (Alps): petrology and geochemistry of subcontinental mantle and Jurassic exhumation during rifting. Ph.D. thesis, ETH Zürich, Switzerland

Müntener O, Hermann J (1996) The Val Malenco lower crust: upper mantle complex and its field relations (Italian Alps). Schweiz Mineral Petrogr Mitt 76(3):475–500

Müntener O, Kelemen PB, Grove TL (2001) The role of H_2O during crystallization of primitive arc magmas under uppermost mantle conditions and genesis of igneous pyroxenites: an experimental study. Contrib Mineral Petrol 141(6):643–658

Niida K, Green DH (1999) Stability and chemical composition of pargasitic amphibole in MORB pyrolite under upper mantle conditions. Contrib Mineral Petrol 135:18–40

Nyamai CM, Mathu EM, Opiyo-Akech N, Wallbrecher E (2003) A reappraisal of the geology, geochemistry, structures and tectonics of the Mozambique belt in Kenya, east of the rift system. Afr J Sci Techn 4(2):51–71

Olker B (2001) Entwicklung und Anwendung eines Computerprogrammes zur numerischen Modellierung von Diffusionsprofilen in Mineralkörnern. Ph.D. thesis, University of Heidelberg, Germany

O'Reilly SY, Griffin WL (1987) Eastern Australia: 4000 kilometres of mantle samples. In: Nixon PH (ed) Mantle Xenoliths, vol. Wiley, Chichester, pp 267–280

O'Reilly SY, Griffin WL (1995) Trace-element partitioning between garnet and clinopyroxene in mantle-derived pyroxenites and eclogites: *P–T–X* controls. Chem Geol 121:105–130

Orlando A, Abebe T, Manetti P, Santo AP, Corti G (2006) Petrology of mantle xenoliths from Megado and Dilo, Kenya Rift, Southern Ethiopia. Ofioliti 31(2):71–87

Pearson DG, Canil D, Shirey SB (2003) Mantle samples included in volcanic rocks: xenoliths and diamonds. In: Holland HD, Turrekian KK (eds) Treatise on geochemistry, vol 2. Elsevier, Amsterdam, pp 171–275

Pertermann M, Hirschmann MM, Hametner K, Gunther D, Schmidt MW (2004) Experimental determination of trace element partitioning between garnet and silica-rich liquid during anhydrous partial melting of MORB-like eclogite. Geochem Geophys Geosys 5:Q05A01. doi:10.1029/2003GC000638

Pettke T, Halter WE, Webster JD, Aigner-Torres M, Heinrich CA (2004) Accurate quantification of melt inclusion chemistry by LA–ICP–MS: a comparison with EMP and SIMS and advantages and possible limitations of these methods. Lithos 78(4):333–361

Piccardo GB, Messiga B, Vannucci R (1988) The Zabargad peridotite-pyroxenite association: petrological constraints on its evolution. Tectonophys 150(1–2):135–162

Righter K, Carmichael ISE (1993) Mega-xenocrysts in alkali olivine basalts: fragments of disrupted mantle assemblages. Am Mineral 78(11–12):1230–1245

Rivalenti G, Mazzucchelli M, Vannucci R, Hofmann AW, Ottolini L, Bottazzi P, Obermiller W (1995) The relationship between websterite and peridotite in the Balmuccia peridotite massif (NW Italy) as revealed by trace-element variations in clinopyroxene. Contrib Mineral Petrol 121(3):275–288

Sen C, Dunn T (1995) Experimental modal metasomatism of a spinel lherzolite and the production of amphibole-bearing peridotite. Contrib Mineral Petrol 119(4):422–432

Shaw CSJ, Eyzaguirre J (2000) Origin of megacrysts in the mafic alkaline lavas of the West Eifel volcanic field, Germany. Lithos 50(1–3):75–95

Sobolev AV, Hofmann AW, Sobolev SV, Nikogosian IK (2005) An olivine-free mantle source of Hawaiian shield basalts. Nature 434(7033):590–597

Suhr G (1999) Melt migration under oceanic ridges: inferences from reactive transport modelling of upper mantle hosted dunites. J Petrol 40(4):575–599

Tabit A, Kornprobst J, Woodland AB (1997) The garnet peridotites of the Beni Bousera massif (Morocco): tectonic mixing and iron–magnesium interdiffusion. CR Acad Sci II A 325(9):665–670

Ulianov A, Kalt A (2006) Mg–Al sapphirine- and Ca–Al hibonite-bearing granulite xenoliths from the Chyulu Hills Volcanic Field, Kenya. J Petrol 47(5):901–927

Ulianov A, Kalt A, Pettke T (2006) Aluminous websterite and granulite xenoliths from the Chyulu Hills volcanic field, Kenya: gabbro-troctolitic cumulates subjected to lithospheric foundering. Contrib Mineral Petrol 152(4):459–483

Ulmer P (2001) Partial melting in the mantle wedge: the role of H_2O in the genesis of mantle-derived 'arc-related' magmas. Phys Earth Planet In 127(1–4):215–232

Van der Wal D, Vissers RLM (1996) Structural petrology of the Ronda peridotite, SW Spain: deformation history. J Petrol 37(1):23–43

Vannucci R, Shimizu N, Piccardo GB, Ottolini L, Bottazzi P (1993) Distribution of trace elements during breakdown of mantle garnet: an example from Zabargad. Contrib Mineral Petrol 113:437–449

Volker F (1990) Geochemie der quartären Vulkanite auf der Ostschulter des Kenia-Rifts. Ph.D. thesis, University of Karlsruhe, Germany

Wilkinson JFG, Stolz AJ (1997) Subcalcic clinopyroxenites and associated ultramafic xenoliths in alkali basalt near Glen Innes, northeastern New South Wales, Australia. Contrib Mineral Petrol 127(3):272–290

Wilshire HG, Shervais JW (1975) Al-augite and Cr-diopside ultramafic xenoliths in in basaltic rocks from the Western United States. Phys Chem Mineral 9:257–272

Winn RD, Steinmetz JC, Kerekgyarto WL (1993) Stratigraphy and rifting history of the mesozoic-cenozoic Anza rift, Kenya. AAPG Bull 77:1989–2005

Xiong XL, Adam J, Green TH (2005) Rutile stability and rutile/melt HFSE partitioning during partial melting of hydrous basalt: implications for TTG genesis. Chem Geol 218(3–4):339–359

Zanetti A, Mazzucchelli M, Rivalenti G, Vannucci R (1999) The Finero phlogopite–peridotite massif: an example of subduction-related metasomatism. Contrib Mineral Petrol 134:107–122